Unimolecular and bimolecular formic acid decomposition routes on dispersed Cu nanoparticles

Ting Chun Lin[1,2], Unai De La Torre[1], Ava Hejazi[1], Stephanie Kwon[1,3,*], Enrique Iglesia[1,*]

[1]Department of Chemical and Biomolecular Engineering, University of California, Berkeley, California 94720, United States

[2]Department of Chemical Engineering and Materials Science, University of Minnesota-Twin Cities, Minneapolis, Minnesota 55455, United States

[3]Department of Chemical and Biological Engineering, Colorado School of Mines, Golden, Colorado 80401, United States

** Corresponding author: kwon@mines.edu, iglesia@berkeley.edu*

Key words: Formic acid, Dehydrogenation, Copper, Density functional theory, Kinetic analysis

Abstract

The elementary steps and site requirements in formic acid (HCOOH) dehydrogenation on Cu surfaces remain of keen interest because formate species act as intermediates or spectators in methanol synthesis and water-gas shift reactions. Steady-state and transient kinetic data, isotopic effects, infrared spectra during catalytic and stoichiometric reactions, and theoretical treatments based on density functional theory (DFT) provide evidence for bimolecular reactions, in which saturated bidentate formate (*HCOO*) adlayers, present at 0.25 ML (0.25 *HCOO* per Cu surface atom), react with undissociated species (HCOOH□) bound at interstices within formate adlayers (□) to form H-bonded bimolecular HCOOH□-*HCOO* adducts. The co-existence of vicinal HCOOH□ and *HCOO* moieties is evident from antisymmetric infrared bands for *HCOO* that become stronger as a result of their H-bonding that perturbs the induced dipole moment of *HCOO* upon vibration, consistent with DFT-derived vibrational frequencies and intensities for such perturbed species. The *HCOO* moiety in this complex undergoes C-H activation via a transition state that is preferentially stabilized through H-bonding with the vicinal HCOOH□ relative to its *HCOO* precursor. DFT-derived HCOOH dehydrogenation activation barriers and those determined from the evolution of CO_2 from pre-adsorbed *HCOO* species are about 10 kJ mol^{-1} smaller in the presence of gaseous HCOOH reactants (because of HCOOH□-*HCOO* interactions) than those for the unimolecular decomposition of bound *HCOO* species. Such bimolecular routes are consistent with measured effects of HCOOH, H_2, and CO pressures and of H/D isotopic substitution on dehydrogenation turnover rates and represent the predominant channel for the formation of CO_2 and H_2 during catalytic HCOOH dehydrogenation on Cu nanoparticles. A saturated *HCOO* adlayer that retains binding interstices and the presence of HCOOH(g) enable a sequence of elementary steps unavailable for *HCOO* species, thus circumventing unassisted unimolecular routes that exhibit higher activation barriers.

1. Introduction

HCOOH dehydrogenation is an attractive route to produce H_2 on demand as reactants in electricity generation through fuel cells [1] because of its high hydrogen density and its potential provenance from biogenic feedstocks [2]. These applications require a very high dehydrogenation selectivity because the CO formed via HCOOH dehydration or secondary reverse water-gas shift reactions strongly inhibits electrocatalysis at fuel cell electrodes. Supported Cu nanoparticles have garnered interest as they exclusively form H_2 and CO_2 from HCOOH without detectable CO products [3,4]. The mechanism of HCOOH dehydrogenation catalysis on Cu is also relevant for understanding those of water-gas shift [5–7] and methanol synthesis [8–10], reactions that involve bound formate species as reactive intermediates or spectators. Such practical and fundamental matters have led to several experimental and theoretical studies of HCOOH dehydrogenation on Cu catalysts as dispersed nanoparticles [11–13] and as extended single crystal surfaces [4,14,15]. The methods used to identify reactive intermediates and elementary steps have included kinetic analysis [13,16], transient reaction studies of pre-adsorbed formate (temperature-programmed surface reaction; TPSR) [3,4,17,18], *in situ* infrared spectra [19–21], and density functional theory (DFT) treatments of the energies of bound species and their elementary interconversion steps [22–26].

HCOOH binds dissociatively on Cu surfaces to form bidentate formate species (*HCOO*) at vicinal Cu atoms and bound H-atoms (H*) [19,20]. Transient studies have shown that bound H* species recombine and desorb as H_2(g) below ambient temperatures from Cu(110) surfaces after HCOOH pre-adsorption at 200 K [4]. The stranded *HCOO* species subsequently decompose at about 460 K to form CO_2 and H_2 at decomposition rates that are limited by C-H bond cleavage in the bound formates, as indicated by similar CO_2 and H_2 evolution profiles measured from HCOOD and HCOOH [4] and CO_2 evolution profiles that are higher in temperature for the decomposition of pre-formed *DCOO* than that of pre-formed *HCOO* [17,18]. Measured activation barriers on Cu(110) (133 kJ mol^{-1}) were similar when *HCOO* coverages were varied by more than an order of magnitude, demonstrating that the reactivities of *HCOO* species are not very sensitive to their coverages [4,18]. These barriers resemble those measured for the decomposition of pre-adsorbed formates on Cu/SiO_2 (133 kJ mol^{-1}) and Cu powders (116-123 kJ mol^{-1}) and for the decomposition of crystalline Cu formate powders (125 kJ

mol^{-1}) [3,16], indicative of C-H cleavage steps that are not strongly influenced by the identity of the exposed facets.

Measured activation barriers for HCOOH dehydrogenation rate constants in the zero-order regime (i.e., at coverages of HCOOH-derived species that do not depend on HCOOH pressure) are smaller during catalytic HCOOH decomposition on Cu/SiO_2 (97 kJ mol^{-1}) than during the decomposition of pre-adsorbed *HCOO* species on the same sample (133 kJ mol^{-1}) [12]. These data led to the proposal that gaseous or weakly-bound HCOOH species may be able to assist *HCOO* decomposition [12]. Such bimolecular HCOOH decomposition routes were not examined by theory, which only considered low *HCOO* coverages (≤ 1/9 monolayer (ML)) [22–25]. A more recent DFT study, carried out without the corrections for dispersion forces essential to describe the energies of weakly-bound species, suggested that the presence of co-adsorbed HCOOH on Cu surfaces can stabilize the C-H activation transition state (TS) for *HCOO* decomposition through strong H-bonding [26]. The calculated activation barriers relevant to the zero-order rate constants (i.e., the energies for the formation of the C-H activation TS from the *HCOO* precursor), however, were similar for *HCOO* decomposition with and without the presence of the co-adsorbed HCOOH species (88 vs. 87 kJ mol^{-1} for Cu(111); electronic energies without zero-point energy corrections) because the H-bonding influences the energies of TS and *HCOO* precursor to a similar extent [26], in contradiction with the previous proposal based on experimental measurements [12]. Another recent work based on dispersion-corrected DFT calculations and microkinetic modeling, presented by the same authors, also contradicts these previous conclusions by proposing that HCOOH dehydrogenation on Cu surfaces can occur in parallel via both unimolecular and bimolecular routes, where their relative contributions depend on reaction temperatures and HCOOH pressures [27].

The results reported here were obtained by combining kinetic, isotopic, spectroscopic, transient, and dispersion-corrected DFT analyses to demonstrate that unimolecular *HCOO* decomposition routes, prevalent for *HCOO* decomposition in the absence of gaseous HCOOH reactants and at low *HCOO* coverages, occur along with the more facile bimolecular routes mediated by *HCOO* interactions with more weakly-bound HCOOH species. In fact, Cu surfaces remain saturated with *HCOO* species at all practical conditions (0.1-3.5 kPa HCOOH; 473-503 K) with the coverage of *HCOO* species reaching saturation at 1/4 ML (*HCOO*/$Cu_{surface}$=1/4) because of strong repulsion among bound *HCOO* species at higher

coverages. HCOOH molecules may additionally bind at interstitial sites (□) within these strongly-bound *HCOO* adlayers to form molecularly-bound HCOOH□ species that promote the decomposition of the vicinal *HCOO* by stabilizing the C-H activation TS more effectively than it is able to stabilize the *HCOO* precursor via H-bonding. As a result, measured turnover rates reflect bimolecular decomposition of HCOOH□-*HCOO* complexes rather than unimolecular *HCOO* decomposition.

The results and conclusions of this work provide a compelling example of how repulsive interactions among bound species restrict coverages to < 1 ML, thus allowing residual interstices in this "passivated" surface to bind intermediates less strongly and, consequently, enable them to react or to increase the reactivity of the bound species in the more refractory template. In fact, few reactions of molecules that bind strongly on surfaces would be able to occur at detectable rates without the perturbations and "shoving" imposed by the discomfort caused by intermolecular repulsion as surfaces approach saturation in the presence of gaseous (or liquid) reactants. Such effects are evident for HCOOH dehydration on TiO_2 surfaces [28] and for reactions of H_2-CO mixtures on Ru nanoparticles [29]; in the latter case, H_2-CO reactions would not have occurred at practical (or even detectable) rates in the absence of the ubiquitous discomfort characteristic of surfaces at near CO saturation coverages. Indeed, catalysis in practice benefits from the complexity inherent in non-Langmuirian kinetics, which cannot be captured by model systems at low coverages or by theoretical treatments that ignore such non-idealities in search of computational efficiency, but at the expense of their relevance to practical catalysis. Theory, spectroscopy, and kinetic analyses must be combined to rigorously evaluate and identify the plausible mechanisms that accurately describe reactions on saturated surfaces. Bimolecular reactions are, in fact, the norm and not the exception on the crowded surfaces that prevail in the practice of surface catalysis.

2. Methods

2.1 Catalyst synthesis and treatment protocols

Cu/SiO_2 (5, 10, 20% wt. Cu) samples were prepared using homogeneous deposition-precipitation methods mediated by pH changes caused by the hydrolysis of urea [30]; the Cu contents were varied by changing the mass ratios of $Cu(NO_3)_2 \cdot 2.5H_2O$ (Sigma-Aldrich) and colloidal SiO_2 (30 % wt. in H_2O; Sigma-Aldrich) precursors. These reagents were then combined

with urea ($CO(NH_2)_2$) (Urea:Cu^{2+} = 3:1; Sigma-Aldrich) and dissolved in deionized (DI) water (≥ 17.6 MΩ-cm resistivity). A 0.5 M HNO_3 solution (diluted from 70% HNO_3; Sigma-Aldrich) was added slowly to the slurry to achieve a pH of ~2. This mixture was heated from ambient temperature to 363 K (0.167 K s^{-1}) while stirring (12 Hz) and held at 363 K for 20 h under complete reflux. The solids were recovered by vacuum filtration and rinsed with deionized water (≥ 17.6 MΩ-cm) until the filtrate reached a pH value of 7; these solid samples were then dried at 383 K in static ambient air (> 12 h). The recovered powders were treated sequentially (i) in flowing dry air (Praxair; 99.999%; 1.67 $cm^3\ g^{-1}\ s^{-1}$) by heating from ambient temperature to 723 K at 0.167 K s^{-1} and holding for 5 h before cooling down to ambient temperature, (ii) in flowing 10% H_2/He (H_2, Praxair; 99.95%; He, Praxair; 99.999%; 5.56 $cm^3\ g^{-1}\ s^{-1}$) by heating from ambient temperature to 573 K at 0.033 K s^{-1} and holding for 2 h before cooling down to ambient temperature, and (iii) in flowing 1% O_2/He (O_2/He, Praxair; 2.02% O_2; He, Praxair; 99.999%; 0.83 $cm^3\ g^{-1}\ s^{-1}$) at ambient temperature for 1 h to prevent exothermic oxidation upon exposure to ambient air. The samples and transfer lines were purged with He (Praxair; 99.999%; 5.0 $cm^3\ g^{-1}\ s^{-1}$) for ~0.3 ks between each treatment condition to prevent H_2 and O_2 mixing.

2.2 Copper metal contents and nanoparticle dispersions

Cu contents in Cu/SiO_2 samples were confirmed by inductively-coupled plasma emission spectroscopy (ICPES; Perkin Elmer 5300 DV). The number of exposed Cu atoms in Cu nanoparticles was measured using the N_2O titration methods; neither O_2 nor H_2 molecules serve as selective titrants for surface Cu atoms because O_2 molecules form multiple oxygen layers at ambient temperature, while H_2 molecules only cover a fraction of the surface (< 0.1 ML) [31]. Cu dispersions, defined as the fraction of atoms exposed at Cu nanoparticles, were determined using N_2O uptakes and a N_2O: $Cu_{surface}$ stoichiometry of 1:2 [32]. Samples (0.16-0.35 g) were held within a U-shaped quartz reactor (4 mm inner diameter) and treated in flowing 20% H_2/He (3.33 $cm^3\ s^{-1}$) by heating from ambient temperature to 573 K at 0.033 K s^{-1} and holding for 2 h before cooling down to 303 K. The system was then flushed with He (3.33 $cm^3\ s^{-1}$) at 303 K for 1 h, heated to 353 K at 0.033 K s^{-1} and held for another 1 h before introducing N_2O as a 0.15% N_2O/0.15% Ar/He mixture (3.0% N_2O/3.0% Ar, Praxair; 99.999%; He, Praxair; 99.999%; 1.66 $cm^3\ g^{-1}\ s^{-1}$) while measuring the composition of the effluent with an on-line infrared gas analyzer

(MKS; MultiGas Series 2000). The mean Cu nanoparticle diameters (5.0, 9.8, and 12.2 nm for 5, 10, and 20% wt. Cu/SiO_2, respectively) were calculated based on these measured Cu dispersions [33,34]; the results from N_2O uptake measurements and the calculation details are discussed in Section S1 (Supplemental Information (SI)).

2.3 Steady-state catalytic HCOOH dehydrogenation rate measurements

HCOOH dehydrogenation rates (0.1-3.5 kPa HCOOH; 473-503 K) were measured on Cu/SiO_2 samples of 125-180 μm aggregate diameters. Samples (0.3-1.6 mg) were held within a U-shaped quartz reactor (4 mm inner diameter) and diluted with inert quartz powders (0.4 g; Sigma-Aldrich; acid-washed with 1 M HNO_3 at ambient temperature, vacuum filtered, rinsed with DI H_2O, and dried in flowing dry air at 373 K for 12 h) in order to achieve bed heights required for plug-flow hydrodynamics. Diluent quartz powders did not show detectable HCOOH decomposition products at the conditions of these catalytic rate measurements. Intra-aggregate mixtures of quartz powders and 20% wt. Cu/SiO_2 with 27-50 mass ratios were prepared by grinding them together, pelleting, and sieving to retain 125-180 μm aggregates. Measured HCOOH dehydrogenation rates were unaffected by intraparticle dilution (Cu/SiO_2:quartz = 1:27 and 1:50 mass ratios; Fig. S2; SI), confirming the absence of heat and mass transfer corruptions of measured rates. All Cu samples were treated in 20% H_2/He (1.67 $cm^3\ s^{-1}$) by heating from ambient temperature to 573 K at 0.033 K s^{-1} and holding for 2 h before cooling down to reaction temperatures; the system was then flushed with flowing He for at least 0.5 h at the reaction temperature before introducing the reactant mixtures.

Bed temperatures were maintained using resistive heating and an electronic controller (Watlow; Series 982) and measured with a thermocouple (K-type; Omega) placed within a dimple at the outer reactor wall. Inlet molar rates were controlled using individual mass flow controllers (Porter; Model 201) and adjusted to maintain target molar inlet rates and the pressures of He, H_2 (Praxair; 99.999%), and CO (Praxair; 90%; Ar balance). HCOOH (Sigma-Aldrich; ≥ 98%; used without further purification), and its isotopologues (DCOOH and DCOOD, Cambridge Isotope Laboratories; ≥ 98% chemical and isotopic purities for both) were introduced as a liquid into a flowing gas stream using a syringe micropump (Cole Parmer; 74900 series) and vaporized at 323 K. All transfer lines, except for those near the injection port, were kept at

ambient temperature to prevent HCOOH decomposition within the heated stainless steel lines; consequently, HCOOH pressures were kept below its vapor pressure at ambient temperature (5.3 kPa for HCOOH [35] at 298 K) to prevent its condensation within transfer lines.

The concentrations of the reactant (HCOOH), products (H_2 and CO_2), and CO in the effluent stream were measured using a gas chromatography system (Agilent; 6890A), equipped with a packed column (Agilent; Porapak-Q; 4.8 m; 80-100 mesh) and a thermal conductivity detector (TCD). Molecular speciation and response factors were determined using known standards. HCOOH and its isotopologues (DCOOH and DCOOD) were speciated by on-line mass spectrometry (MKS Spectra; MiniLab LM80) to confirm the isotopic purity of the reactants and the extent to which intramolecular scrambling occurred during HCOOH decomposition turnovers.

HCOOH conversions in some of the kinetic measurements were higher than those required for differential conversion analysis (> 10%) even at very low catalyst loadings (0.3-1.6 mg) and after intra-aggregate dilution with quart powders (1:27-50 mass ratios), thus causing HCOOH concentration gradients along the catalyst bed. The reported turnover rates are those at zero conversion, extrapolated using the integrated form of the rate equation and the regressed rate and equilibrium constants in order to accurately account for the effects of HCOOH concentration gradient on rates (analysis and regression details in Section S3; SI); without such extrapolations, rates are reported as site-time yields, which reflect the measured rates normalized by the number of exposed Cu sites within the reactor.

2.4 Transient reaction studies of pre-adsorbed HCOOH-derived species

TPSR experiments were conducted using the reactor system described in Section 2.3. Temperatures were monitored using a K-type thermocouple placed within a dimple at the outer reactor wall near the catalyst bed and recorded using a temperature logger (National Instruments; USB-TC01). Samples (0.085-0.3 g) were treated in 20% H_2/He (1.67 cm^3 s^{-1}) by heating the samples from ambient temperature to 573 K at 0.033 K s^{-1} and holding for 2 h before cooling down to 348 K. The system was then flushed with flowing He or H_2 (1.67 cm^3 s^{-1}) for > 0.5 h before introducing 0.5 kPa HCOOH (He or H_2 balance; 1.67 cm^3 s^{-1}) at 348 K. Samples were contacted with HCOOH until the effluent reached 0.5 kPa HCOOH, as measured by an on-line

infrared analyzer (MKS; MultiGas Series 2000). The samples were subsequently flushed at 348 K with flowing He or H_2 (1.67 cm^3 s^{-1}) for > 0.5 h until HCOOH(g) was no longer detected in the effluent in order to remove any physisorbed HCOOH species, before heating to 673 K at a ramping rate of 0.083 K s^{-1}.

2.5 *In situ* infrared spectroscopy

Infrared spectra were collected using Cu/SiO_2 wafers (~10 mg cm^{-2}) held between KBr windows within a quartz cell. Temperatures were maintained by external resistive heating, monitored using a thermocouple (Omega; K-type) held in a dimple at the outer reactor wall near the outer edge of the wafer and controlled with an electronic temperature controller (Watlow; Series 982). Inlet molar rates and concentrations of reactant mixtures were set by mass flow controllers and a syringe micropump (as described in Section 2.3). Spectra were collected in transmission mode (ThermoNicolet; Nexus 670; Hg-Cd-Te (MCT) detector) and the effluent stream was concurrently analyzed by an on-line infrared analyzer (MKS; MultiGas Series 2000).

Cu/SiO_2 wafers were treated in 20% H_2/He (1.67 cm^3 s^{-1}) by heating from ambient temperature to 573 K at 0.033 K s^{-1} and holding for 2 h before cooling to 453 K. The system was flushed with He (6.67 cm^3 s^{-1}) at 453 K and the background spectra were collected before introducing HCOOH to the reactant stream (3 kPa HCOOH; He balance; 6.67 cm^3 s^{-1}); these experiments were performed at lower temperature (453 K) than steady-state measurements (473-503 K) to minimize HCOOH conversions within the Cu/SiO_2 pellets and to maintain differential HCOOH conversions. Spectra were collected during catalytic HCOOH decomposition and after removing HCOOH(g) from the reactant stream. Spectra were also obtained during TPSR measurements. In these experiments, treated Cu/SiO_2 wafers were first flushed with flowing He (6.67 cm^3 s^{-1}) at 453 K and the background spectra were collected. HCOOH (0.5 kPa; H_2 balance; 5.0 cm^3 s^{-1}) was then introduced at 348 K until the effluent composition reached steady-state, as monitored by on-line infrared analysis. HCOOH was then removed from the reactant stream and the system was flushed with H_2 (5.0 cm^3 s^{-1}) until HCOOH(g) was undetectable in the effluent, after which the temperature was increased to 673 K (0.083 K s^{-1}). All infrared spectra were collected in the 1000-4000 cm^{-1} range with a resolution of 2 cm^{-1} by averaging 64 scans, except during transient experiments, for which 4 scans were averaged to obtain each spectrum in order to achieve the requisite temporal resolution.

2.6 Computational methods

The energies of plausible intermediates and transition states involved in HCOOH dehydrogenation elementary steps were estimated on periodic Cu(111) facets, found to be the surfaces predominantly exposed at Cu nanoparticle surfaces [15]. Periodic DFT calculations were performed using the Vienna ab-initio simulation package (VASP) [36]. The revised Perdew-Burke-Ernzerhof (RPBE) [37,38] functionals within the generalized gradient approximation (GGA) were used, which provide computationally efficient methods to probe the energies of all intermediates and transition states involved in complex bimolecular pathways. Such functionals accurately predict the standard enthalpy of HCOOH dehydrogenation reaction ($HCOOH(g) \rightarrow CO_2(g) + H_2(g)$, ΔH^0 = -15 vs. -19 kJ mol^{-1} from gas-phase enthalpies from the NIST database and from theory; Table S2; SI) and are widely used in the literature to assess HCOOH dehydrogenation catalysis on transition metal surfaces [22–24,26,39,40]. Dispersive interactions, essential to determine energies for the weakly-bound species that mediate bimolecular routes, were calculated using the Grimme's D3 method [41,42] at each energy iteration. The energies of intermediates and transition states calculated with such RPBE-D3 methods are benchmarked against those calculated with PW91, the other widely-used GGA functionals [22,26]; these results are discussed in the supporting information (Section S8; SI). In both cases, plane-wave basis sets were constructed using an energy cutoff of 396 eV with core electrons treated using projector-augmented wave (PAW) methods [43]. A Monkhorst–Pack 13 × 13 × 13 grid was used for bulk calculations and a 5 × 5 × 1 grid was used for all slab models. Electronic structures were converged to < 10^{-6} eV between successive iterations.

The lattice parameters for bulk Cu metal derived with RPBE-D3 (0.357 nm) and PW91 (0.363 nm) methods were similar to the experimental value (0.361 nm; [44]); these DFT-derived lattice parameters were used with each DFT method to construct Cu(111) slab models consisting of four Cu layers. All atoms, including bound species, were fully relaxed until all forces were < 0.05 eV $Å^{-1}$, except for the Cu atoms at the bottom two layers, which were kept at their bulk positions. A 2 nm vacuum layer was placed between the slabs in the z-direction to minimize the interactions among repeating images. The energies of intermediates and transition states involved in the unimolecular routes were calculated using a (4x4) supercell (16 Cu atoms per layer) with 1 HCOOH(g) molecule, representing a 1/16 ML, with minimal adsorbate-adsorbate interactions.

Bimolecular routes were probed using a (4x4) supercell containing 4 *HCOO* species (at the maximum 1/4 ML *HCOO* coverage) with 1 HCOOH(g) molecule.

Minimum energy paths connecting reactant, intermediate, and product states were calculated for each proposed elementary step using nudged elastic band (NEB) methods [45] with 8-16 images and a convergence criteria of 1 x 10^{-4} eV for energies and 0.1 eV $Å^{-1}$ for forces on all unconstrained atoms. Structures at the maximum energy along the reaction coordinate (derived from NEB calculations) were used as the starting points for refining TS structures using the Henkelman's Dimer method [46] with convergence criteria of 1 x 10^{-6} eV for electronic energies and 0.05 eV $Å^{-1}$ for forces.

Vibrational frequencies of each intermediate and TS structure were derived from the mass-weighted force constant matrix (the Hessian matrix), where the force constant derivatives were calculated from the finite differences of the forces upon atomic displacement of ±0.015 Å in Cartesian coordinates. The intensity of each vibrational mode (i) was determined by calculating the square of the dynamic dipole moment of its mode ($\partial\mu/\partial Q_i$) [47], derived from the dipole moment change in the direction perpendicular to the slab with respect to the distance for the perturbation of atoms along each mode (Q_i) [48], using the code developed for this purpose [49,50]. The intensity versus frequency delta functions were broadened using Lorentzian functions (of width 20 cm^{-1}) and infrared spectra were generated by summing such functions over all modes.

Zero-point vibrational energy (ZPVE) corrections and vibrational energies at each temperature were calculated using statistical mechanical formalisms [51] and DFT-derived vibrational frequencies. Low-frequency vibrational modes are the predominant contributors to entropies, but they cannot be accurately described using harmonic oscillator models, thus introducing significant errors in entropy calculations. These modes resemble frustrated translational and rotational modes that become restricted in bound species. The contributions of these low modes to vibrational entropies were replaced by a fraction (0.7) of the translational and rotational entropies of the respective molecules in the gas-phase, as inferred empirically from measured adsorption entropies of weakly-bound species on oxide surfaces [52]. ZPVE and thermal contributions to enthalpies and free energies from vibrational modes (and translational and rotational modes for gas-phase molecules) were added to dispersion-corrected DFT-derived electronic energies to estimate enthalpies and free energies of gas-phase molecules, bound

intermediates, and transition states at relevant reaction temperatures; all free energies were calculated at the standard pressure (1 bar).

3. Results and discussion

3.1 Steady-state HCOOH dehydrogenation on Cu catalysts and kinetic isotope effects

HCOOH dehydrogenation rates were measured on 5% wt. Cu/SiO_2 catalysts over a range of HCOOH pressures (0.1-3.5 kPa; 473-503 K) (Fig. 1). CO_2 and H_2 were the only products detected at all conditions. Rates increased linearly at low HCOOH pressures and then sublinearly as HCOOH pressure increased. The deviations from linearity shifted to lower HCOOH pressures with decreasing temperature, as expected from the higher coverages of bound intermediates at lower temperatures for each given HCOOH pressure. The addition of H_2 to the inlet stream did not influence rates (Fig. 2). The extent of formic acid conversion (1.1-3.7 %; 2.0 kPa DCOOD; 493 K), modulated by DCOOD space velocity in this case, did not influence rates, indicating neither CO_2 nor D_2 inhibit dehydrogenation rates (Fig. S3; SI). Turnover rates (per surface Cu atom) were similar on all Cu/SiO_2 catalysts (5 vs. 20% wt.; 0.1-3.5 kPa HCOOH; 503 K; Fig. S4; SI), in spite of their different mean nanoparticle diameters (5.0 vs. 12.2 nm from N_2O titration, respectively), indicative of weak effects of Cu nanoparticle size on surface reactivity within the size range examined (5.0-12.2 nm) used in this study; the effects of HCOOH and H_2 pressures on rates are shown for 20% wt. Cu/SiO_2 in Figure S5 (SI). These weak effects of mean Cu nanoparticle sizes are consistent with those evident from the similar barriers for HCOOH dehydrogenation measured on Cu powders, Cu/SiO_2, and Cu/Al_2O_3 catalysts (5-1000 nm mean diameter) [12].

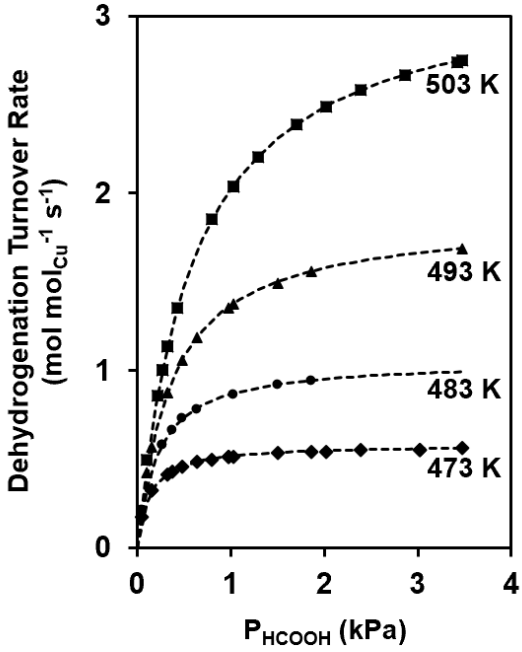

Figure 1. HCOOH dehydrogenation turnover rates (per surface Cu atom) measured on Cu/SiO_2 (5% wt.) as a function of HCOOH pressure (0.1-3.5 kPa; 473-503 K). Dashed curves represent the optimal regression of rates using the functional form of Equation 4 (Sec. S3; SI).

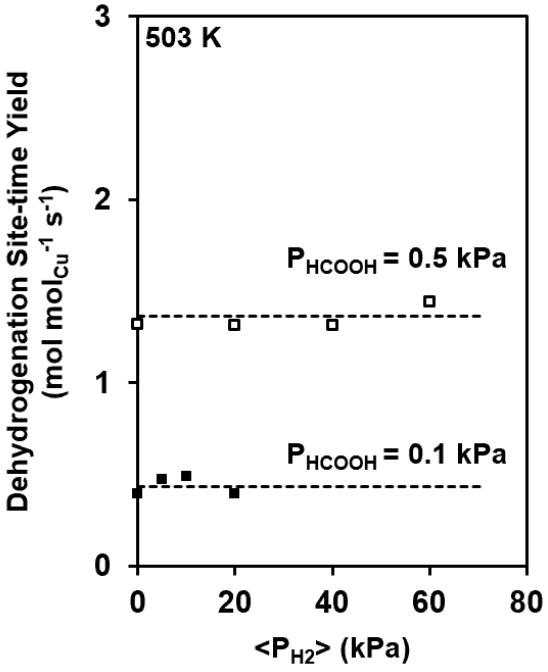

Figure 2. HCOOH dehydrogenation site-time yields (per exposed Cu atom) measured with H_2 co-feed on Cu/SiO_2 (5% wt.) as a function of averaged H_2 pressure (0-60 kPa; 0.1 and 0.5 kPa HCOOH; 503 K). The dashed lines represent the trend lines.

Scheme 1. Proposed sequence of elementary steps for unimolecular HCOOH dehydrogenation.

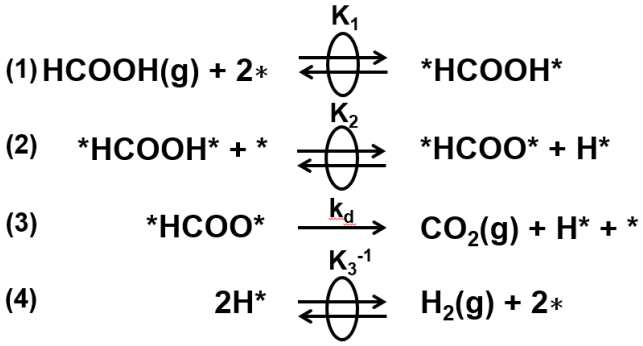

[a]Quasi-equilibrated steps are denoted by ovals in double arrows.

Unimolecular HCOOH dehydrogenation routes proceed via a bidentate formate (*HCOO*) bound at two adjacent Cu atoms and a surface bound hydrogen atom (H*) formed from quasi-equilibrated O-H activation in molecularly bound HCOOH (*HCOOH*; steps 1 and 2; Scheme 1) [4,16]. *HCOO* species form CO_2 via a kinetically-relevant C-H activation step (step 3; Scheme 1). The resulting H* atoms recombine and desorb as H_2(g) in quasi-equilibrated steps (step 4; Scheme 1). Such steps and the reversibility assumptions are consistent with H_2 and CO_2 evolution profiles measured upon exposure of Cu(110) to HCOOH(g) at 200 K and heating to 523 K [4]. Fast *HCOO* formation is evident from H_2 evolution at 270 K in amounts consistent with the stoichiometric formation of *HCOO* (H_2:*HCOO* = 1:2) [4]. *HCOO* species react at about 460 K to form CO_2* and H* species that immediately desorb as CO_2(g) and H_2(g) at rates limited by C-H activation in *HCOO* [18]. The kinetic irrelevance of the O-H activation in HCOOH (steps 1 and 2; Scheme 1) is consistent with the similar dehydrogenation rates measured for DCOOH and DCOOD reactants (Fig. 3); both of these rates were lower than those for HCOOH, consistent with C-H activation in *HCOO* as the sole kinetically-relevant step (step 3; Scheme 1). A rigorous analysis of kinetic isotope effects (KIE) on rate parameters (and their comparisons to DFT-derived values) requires the regression of rate data for each isotopologue in order to estimate their respective rate constants, as described below.

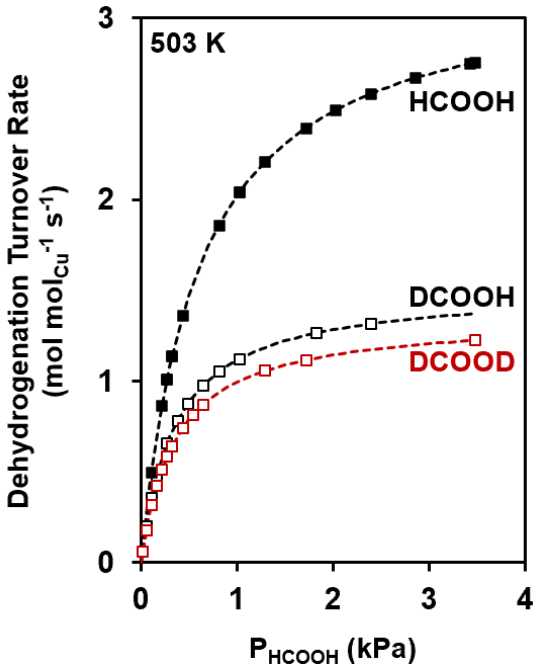

Figure 3. Dehydrogenation turnover rates of HCOOH, DCOOH, and DCOOD (per exposed Cu atom) on Cu/SiO_2 (5% wt.) as a function of formic acid pressures (0.1-3.5 kPa; 503 K). Dashed curves represent the optimal regression of rates using the functional form of Equation 4 (Sec. S3; SI).

The sequence of elementary steps in Scheme 1 leads to HCOOH dehydrogenation rates (r_d; per surface Cu atom) given by (derivation in Section S2; SI):

$$r_d = \frac{4\frac{k_d K_1 K_2 P_{HCOOH}}{\sqrt{K_3 P_{H_2}}}}{\left[\left(1+\sqrt{K_3 P_{H_2}}\right)+\sqrt{\left(1+\sqrt{K_3 P_{H_2}}\right)^2+8\frac{K_1 K_2 P_{HCOOH}}{\sqrt{K_3 P_{H_2}}}}\right]^2} \quad (1)$$

K_1, K_2, k_d, and K_3 represent the equilibrium and rate constants for the respective elementary steps in Scheme 1. At high *HCOO* coverages (set by quasi-equilibrated steps 1, 2 and 4; Scheme 1), Equation (1) becomes:

$$r_d = \frac{k_d}{2} \quad (2)$$

The factor of 2 in Equation 2 accounts for *HCOO* species that occupy two Cu surface atoms. At low *HCOO* and H* coverages (via quasi-equilibrated steps 1, 2 and 4; Scheme 1), Equation 1 becomes:

$$\frac{r_d}{[L]} = \frac{k_d K_1 K_2 P_{HCOOH}}{\sqrt{K_3 P_{H_2}}} \quad (3)$$

This asymptotic rate equation, however, is inconsistent with rates that are insensitive to H_2 pressure (Fig. 2) at conditions where rates vary linearly with HCOOH pressure (< 1 kPa HCOOH; 503 K; Fig. 1). The unimolecular dehydrogenation mechanism (in Scheme 1) thus cannot account for HCOOH dehydrogenation turnover rates on Cu/SiO_2. Such discrepancies, in turn, implicate the plausible involvement of bimolecular routes during catalytic reactions in which HCOOH(g) coexists with bound formate species.

A recent DFT study reported a possible bimolecular route, where co-adsorbed molecularly bound HCOOH facilitates decomposition of vicinal *HCOO* species via strong H-bonding [26]; the calculated activation barriers referenced to the *HCOO* precursor, however, remained the same with and without the presence of the co-adsorbed HCOOH species, possibly because these calculations were carried out without dispersion corrections. The *in situ* infrared spectra and band assignments from simulations described in Section 3.3 confirm the co-existence of molecularly-bound HCOOH and *HCOO* species. Such observations are in agreement with previous experimental work, in which a 1660 cm^{-1} band (for a C=O stretching mode of a molecularly-bound HCOOH) appeared upon re-exposure of a *HCOO*-saturated Cu(100) surface to HCOOH(g) [20]. *HCOO* species, in fact, reach saturation coverages at 1/4 ML, as shown from the amount of CO_2 desorbed during heating of the Cu powders saturated with HCOOH-derived species (0.25 ± 0.05 CO_2 per surface Cu atom) [3]. Higher *HCOO* coverages are prevented by a large kinetic barrier required to form another bidentate formate on Cu surfaces saturated with 1/4 ML *HCOO* ($\Delta G_{503K}^{\ddagger}$ = 135 kJ mol^{-1} to form another bidentate formate from HCOOH(g) on Cu(111) with 1/4 ML *HCOO*). These steps are also thermodynamically unfavorable (ΔG_{503K} = +93 kJ mol^{-1} from HCOOH(g)) because the bidentate formate formed at the interstitial sites (□) experiences repulsive interactions within *HCOO* adlayers, as shown by DFT-derived free energies in Section 3.5.2. Additional HCOOH molecules can instead bind molecularly at interstices (□) within adlayers on *HCOO*-saturated

Cu surfaces to form another layer (HCOOH□), thus accounting for the asymptotic behavior of turnover rates at high HCOOH pressures (Fig. 1). Next, we address the possible bimolecular routes involving these co-adsorbed HCOOH□-*HCOO* complexes on *HCOO*-saturated Cu surfaces and their ability to describe the dependence of rates on HCOOH and H_2 pressures and the kinetic effects of isotopic substitutions.

Two plausible sequences of elementary steps involving HCOOH□-*HCOO* complexes are depicted in Scheme 2. Molecular HCOOH species bound at interstitial sites (□) within the *HCOO* adlayer first form a HCOOH□-*HCOO* complex (step 1; Scheme 2). Either one of the two species can then decompose to form CO_2(g) and H_2(g). HCOOH□ decomposes via the concerted cleavage of C-H and O-H bonds, with the Cu surface atom at interstices (□) abstracting the H-atom in the C-H bond and the vicinal *HCOO* abstracting the H-atom in the O-H bond to form *HCOOH* (step 2a; Scheme 2). The bound H□ reacts with the H-atom in the O-H bond in *HCOOH* to form molecular H_2□ species that desorb as H_2(g), thus restoring a *HCOO* moiety and completing the HCOOH dehydrogenation turnover (step 3a; Scheme 2). Step 2b in Scheme 2 describes an alternative reaction mode of HCOOH□-*HCOO* complexes, in which *HCOO* cleaves its C-H bond via reactions with the Cu atoms to which it is bound to form CO_2* species that subsequently desorb as CO_2(g) (step 2b; Scheme 2). The resulting H* reacts with the H-atom in the O-H bond in the vicinal HCOOH□ to form H_2* that desorbs as H_2(g), thus completing the catalytic cycle by re-forming *HCOO* from HCOOH□ (step 3b; Scheme 2).

Scheme 2. Proposed sequences of elementary steps for bimolecular HCOOH dehydrogenation on *HCOO*-saturated Cu via decomposition of HCOOH□ (red) or *HCOO* (blue) moieties in HCOOH□-*HCOO* complexes.

❖ Decomposition of HCOOH□

(1) □ -*HCOO* + HCOOH(g) $\overset{K_{1,b}}{\rightleftharpoons}$ HCOOH□ -*HCOO*

(2a) HCOOH□ -*HCOO* $\xrightarrow{k_{d,b}}$ H□ -*HCOOH* + CO_2(g)

(3a) H□ -*HCOOH* $\overset{K_{3,b}^{-1}}{\rightleftharpoons}$ □ -*HCOO* + H_2(g)

❖ Decomposition of *HCOO*

(1) □ -*HCOO* + HCOOH(g) $\overset{K_{1,b}}{\rightleftharpoons}$ HCOOH□ -*HCOO*

(2b) HCOOH□ -*HCOO* $\xrightarrow{k_{d,b}'}$ HCOOH□ -*H + * + CO_2(g)

(3b) HCOOH□ -*H + * $\overset{K_{3,b}^{-1}}{\rightleftharpoons}$ □ -*HCOO* + H_2(g)

[a]Quasi-equilibrated steps are denoted by ovals in double arrows.

The assumptions of quasi-equilibrated molecular HCOOH adsorption-desorption on □ sites within the *HCOO* adlayer (step 1; Scheme 2), quasi-equilibrated H_2 recombination-dissociation and *HCOO* re-formation steps (steps 3a and 3b; Scheme 2), and irreversible CO_2 formation steps (steps 2a and 2b; Scheme 2) combined with the observed absence of H_2 partial pressure dependency (Fig. 2) lead to CO_2 formation rates (r_d; per surface Cu atom) given by (derivation in S2; SI):

$$r_d = \frac{(k_{d,b} + k_{d,b}')\, K_{1,b} P_{HCOOH}}{4\left(1 + K_{1,b} P_{HCOOH}\right)} = \frac{k_{app}\, K_{1,b} P_{HCOOH}}{4(1 + K_{1,b} P_{HCOOH})} \quad (4)$$

$K_{1,b}$ is the equilibrium constant for step 1 in Scheme 2. $k_{d,b}$ and $k_{d,b}$' are the rate constants for steps 2a and 2b (for HCOOH□ and *HCOO* decomposition pathways, respectively) in Scheme 2. The denominator terms represent the relative coverages of bare interstitial sites (□-*HCOO*) and molecularly-bound HCOOH (HCOOH□-*HCOO*); the factor of 4 accounts for the ¼ ML saturation coverages of *HCOO* within the bidentate adlayer and is consistent with rates being reported on a per mole surface Cu basis as each *HCOO* together with its vicinal interstitial site (□-*HCOO*) occupies a total of 4 surface Cu atoms. Equation 4 accounts for the irrelevance of H_2 adsorption and accurately describes the kinetic effects of HCOOH on HCOOH dehydrogenation rates over a 100-fold range, as shown in the parity plot in Figure 4. We discuss next the isotope effects on rate and equilibrium constants.

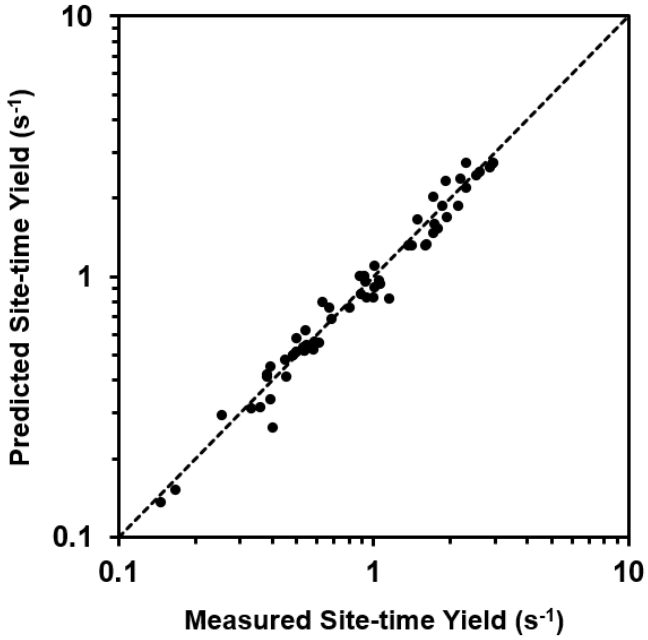

Figure 4. A parity plot between the observed and predicted HCOOH dehydrogenation site-time yields. The predicted rates were obtained using the rate expression shown in Equation 4 and kinetic and thermodynamic parameters regressed from rate data using plug-flow reactor analysis methods (Sec. S3; SI).

The $K_{1,b}$ parameter in Equation 4 represents the equilibrium constant for HCOOH molecular adsorption at interstices within *HCOO* adlayers (□-*HCOO*) to form the HCOOH□-*HCOO* complex (step 1; Scheme 2). Its magnitude reflects the difference in free energy between such a complex ($G_{HCOOH^{\square}-*HCOO*}$) and its HCOOH(g) ($G_{HCOOH(g)}$) and *HCOO* ($G_{\square-*HCOO*}$) precursors:

$$K_{1,b} = \exp\left(-\frac{\Delta G_{1,b}}{RT}\right) = \exp\left[-\frac{\left(G_{HCOOH^{\square}-*HCOO*} - \left(G_{HCOOH(g)} + G_{\square-*HCOO*}\right)\right)}{RT}\right] \quad , \qquad (5)$$

where R is the gas constant. The $k_{d,b}$ and $k_{d,b}$' parameters in Equation 4 represent the rate constants for the decomposition of the HCOOH□ and *HCOO* components in the HCOOH□-*HCOO* complex to form CO_2 products (steps 2a and 2b; Scheme 2). Their values depend on the free energy of formation of the relevant TS ($G^{\ddagger}$) relative to that of the HCOOH□-*HCOO* complex ($G_{HCOOH^{\square}-*HCOO*}$), given by:

$$k_{d,b}\ (or\ \ k_{d,b}') = \frac{N_A RT}{h}\exp\left(-\frac{\Delta G^{\ddagger}}{RT}\right) = \frac{N_A RT}{h}\exp\left[-\frac{(G^{\ddagger} - G_{HCOOH^{\square}-*HCOO*})}{RT}\right] \qquad (6)$$

where N_A is Avogadro constant and h is Planck's constant. The TS structure and its $G^{\ddagger}$ value are different for the two decomposition routes, because they differ in the specific bond rearrangements that mediate each route. The decomposition of the HCOOH□ moiety involves concerted activation of its C-H and O-H bonds (step 2a; Scheme 2), while that of *HCOO* requires only C-H activation via transfer of the H-atom to the surface Cu atom (step 2b; Scheme 2). The $k_{d,b}$ and $k_{d,b}$' constants (and thus the respective $\Delta G^{\ddagger}$ values), however, cannot be measured independently because they appear in rate expressions with an identical functional form; only the apparent rate constant ($k_{app} = k_{d,b} + k_{d,b}$'), accounting for the combined contributions from both routes, can be determined from rate data. The $K_{1,b}$ and k_{app} constants in Equation 4 and the respective enthalpy and entropy components of their Gibbs free energies were obtained by regression of the rate data at different temperatures in Figure 1 to the functional forms of Equations 4-6; these regressed values are compared to the corresponding DFT-derived values in Table 1. DFT-derived enthalpies (after ZPVE corrections and the addition of thermal contributions to dispersion-corrected DFT-derived electronic energies) indicate that the *HCOO* decomposition in the HCOOH□-*HCOO* complex involves a much lower activation barrier than HCOOH□ decomposition ($\Delta H^{\ddagger}$ = 68 vs. 83 kJ mol^{-1}; Table 1). DFT-derived activation barriers for both routes, however, are smaller than measured barriers (109 ± 9 kJ mol^{-1}; Table 1). DFT-derived Gibbs free energies and molecular geometries of intermediates and transition states involved in each bimolecular decomposition route (in Scheme 2), kinetic isotope effects, and their comparisons to experimental values are discussed in Section 3.5.2.

	Exp.[a]	Theory[b]	
$K_{1,b,503K}$ (kPa^{-1})	1.7 ± 0.3		
$\Delta H_{1,b}$ (kJ mol^{-1})	-100 ± 26	-45	
$\Delta S_{1,b}$ (J mol^{-1} K^{-1})	-160 ± 53	-160	
		HCOOH□ decomposition ($k_{d,b}$)	*HCOO* decomposition ($k_{d,b}$')

$k_{app,503K}$ (s^{-1})	13.1 ± 0.9		
$\Delta H^{\ddagger}$ (kJ mol^{-1})	109 ± 9	83	68
$\Delta S^{\ddagger}$ (J mol^{-1} K^{-1})	-10 ± 19	-1	+18

Table 1. Equilibrium and rate constants and the corresponding enthalpies and entropies from kinetic analyses and DFT calculations.

[a]Experimental errors reflect 95% confidence intervals. All kinetic data (0.1-3.5 kPa HCOOH; 473-503 K; Fig. 1) are fitted simultaneously to the functional forms of Equations 4-6 within the ideal plug flow reactor approximations to obtain respective enthalpic and entropic components and corresponding errors. $K_{1,b,503K}$ and $k_{app,503K}$ constants are obtained from regressing the data at 503 K. The regression procedure is detailed in Section S3 (SI). [b]DFT-derived values are calculated at 1/16 ML HCOOH coverage on *HCOO*-saturated Cu(111). DFT results are discussed in detail in Section 3.5.2.

Table 2. Equilibrium and kinetic isotope effects on equilibrium and rate constants from experiments and theory.

	Exp.[a]	Theory[b]	
	$K_{1,b}$		
HCOOH/DCOOH	0.6 ± 0.1	0.8	
HCOOH/DCOOD	0.6 ± 0.1	0.9	
	k_{app}	HCOOH□ decomposition ($k_{d,b}$)	*HCOO* decomposition ($k_{d,b}$')
HCOOH/DCOOH	2.2 ± 0.2	2.6	2.4
HCOOH/DCOOD	2.4 ± 0.2	2.4	2.1

[a]Reported uncertainties represent the standard error. Equilibrium and rate constants ($K_{1,b}$ and k_{app}) for HCOOH and its isotopologues (DCOOH and DCOOD) were obtained by regressing the rate data in Figure 3 to the functional form of Equation 4 within the ideal plug flow reactor approximations. The regression procedure is described in detail in Section S3 (SI).[b] DFT-derived values were calculated at 1/16 ML HCOOH coverage on *HCOO*-saturated Cu(111). Free energies are those at 1 bar HCOOH and 503 K. DFT results are discussed in detail in Section 3.5.2.

Equilibrium and kinetic isotope effects (EIE, KIE) on the $K_{1,b}$ and k_{app} constants are obtained by regressing the rate data for the dehydrogenation of HCOOH and its isotopologues (DCOOH, DCOOD; Fig. 3) using the functional form of Equation 4. EIE values are defined as the ratio of $K_{1,b}$ constants for different isotopologues. These values for HCOOH/DCOOH and HCOOH/DCOOD are both smaller than unity (0.6 ± 0.1; Table 2), consistent with the estimates from DFT calculations (0.8 and 0.9, respectively; Table 2). EIE are dominated by the ZPVE terms and their magnitudes thus depend on the vibrational frequencies of the reactant and product states; the observed inverse EIE reflect vibrational frequency differences between isotopologues that are smaller in the reactant state (HCOOH(g) vs. DCOOH(g) and DCOOD(g))

than in the product state (HCOOH□ vs. DCOOH□ and DCOOD□). Conversely, a normal equilibrium isotope effect is expected for HCOOH/HCOOD from DFT calculations (1.1), because the vibrational frequency differences between the isotopologues in the reactant state (HCOOH(g) vs. HCOOD(g)) are larger than in the product state (HCOOH□ vs. HCOOD□).

KIE values are defined as the ratios of k_{app} for different isotopologues. Such a value for HCOOH/DCOOH is much larger than unity (HCOOH/DCOOH = 2.2 ± 0.2; Table 2) and similar to the value measured for HCOOH/DCOOD (2.4 ± 0.2; Table 2). These observations are consistent with the DFT-derived ratio of $k_{d,b}$ constants for the HCOOH□ decomposition route (step 2a; Scheme 2), which is 2.6 for HCOOH/DCOOH and 2.4 for HCOOH/DCOOD (Table 2). This normal KIE for C-D substitution reflects the C-H vibrational mode that is absent in the C-H activation TS for the HCOOH□ decomposition (step 2a; Scheme 2) but presents in the HCOOH□-*HCOO* precursor as the C-H bond is partially cleaved at the TS. In contrast, the TS includes the O-H bond that is fully formed at the TS; the O-H vibrational mode is thus present at the TS as well as in the HCOOH□-*HCOO* precursor, leading to the weak effects of O-D substitution on measured rates and similar KIE values between HCOOH/DCOOH and HCOOH/DCOOD. DFT-derived ratios of $k_{d,b}$' constants for the *HCOO* decomposition route (step 2b; Scheme 2) also agree well with experimental observations; the ratio of $k_{d,b}$' constants from DFT methods is 2.4 for HCOOH/DCOOH and 2.1 for HCOOH/DCOOD (Table 2). The TS mediating the *HCOO* decomposition (step 2b; Scheme 2) requires only C-H activation in *HCOO* in the complex, leading to a strong KIE for C-D substitution but not for O-D substitution. DFT-derived KIE values are similar between HCOOH□ and *HCOO* decomposition routes (in Scheme 2) and also consistent with measured values within experimental errors[†]. As a result, KIE values cannot be used to discriminate between the two moieties that are able to react in HCOOH□-*HCOO* complexes.

[†] One of the reviewers of the manuscript asserted that HCOOH decomposition follows the unimolecular route as the KIE value obtained based on decomposition of pre-formed *HCOO* and *DCOO* (kH/kD = 2.9 at 460 K) [18] is similar to that measured in the present study during catalytic turnovers, instead of stoichiometric reactions of pre-adsorbed formate. Clearly, the decomposition of pre-formed *HCOO* innately prevents the more facile bimolecular pathways, because it excludes HCOOH(g) and weakly-bound co-adsorbed molecular HCOOH□. The types of experiments in ref. [18] lack the precise bound and gaseous species required to mediate the bimolecular routes and crowded surfaces that circumvent the species and pathways that are the focus of the earlier study. The HCOOH□-*HCOO* complexes that mediate catalytic HCOOH decomposition on Cu nanoparticles can only form in the presence of HCOOH(g) during catalytic turnovers.

The rate equation (Eq. 4) for bimolecular HCOOH dehydrogenation routes (Scheme 2) agrees well with the observed kinetic effects of HCOOH and H_2 pressures and with isotopic substitution on measured rates. This equation was derived by assuming that Cu surfaces are saturated with strongly-bound *HCOO* species at all reaction conditions and that molecular HCOOH adsorption within the *HCOO* layer mediates the bimolecular decomposition channels. In the next section, we compare H* coverages observed during HCOOH catalysis with those expected on clean Cu surfaces to validate the possible saturation of Cu surfaces with *HCOO* during catalytic turnovers. We then compare HCOOH and CO adsorption enthalpies measured during HCOOH catalysis with those measured on clean Cu surfaces in previous studies and those calculated here on clean Cu(111) and *HCOO*-saturated Cu(111) using DFT methods to confirm such hypotheses.

3.2. Adsorption of H_2, HCOOH, and CO molecules on clean and *HCOO*-saturated Cu surfaces

Dissociative H_2 adsorption/desorption steps are equilibrated on Cu surfaces during HCOOH decomposition at 473-503 K; these temperatures are significantly higher than that reported to give reversible adsorption-desorption isotherms (298 K; [53]). As a result, HCOOH dehydrogenation rates are expected to decrease as H* coverages increase with increasing H_2 pressure in the kinetic regime where rates increase linearly with HCOOH pressure (< 1 kPa HCOOH; 503 K; Fig. 1) because of low coverages of HCOOH-derived species. Measured rates, however, remain independent of H_2 pressure even at 60 kPa H_2 (0.5 kPa HCOOH; 503 K; Fig. 2), even though H* species are expected to cover a significant fraction of bare Cu surfaces at such conditions. For instance, the estimated H*-coverage (θ_{H*}) is calculated to be ~0.22 at 60 kPa H_2 (503 K) from experimental dissociative H_2 adsorption enthalpies (-5 kJ mol^{-1}) and pre-exponential factors on Cu(110) (details in Section S4, SI) [54,55].

The absence of H_2 inhibition effects indicates that H*-coverages are, in fact, negligible even at H_2 pressures that would have led to nonnegligible H* coverage on Cu surfaces that remained uncovered by other species. Such observations led us to hypothesize that HCOOH-derived species are present at significant coverages even at low HCOOH pressures (< 1 kPa HCOOH). Yet, dehydrogenation rates were found to be proportional to HCOOH pressures at < 1

kPa HCOOH (Fig. 1), a kinetic behavior that must reflect low coverages of HCOOH-derived surface species required for catalytic turnovers. These data, in turn, led us to infer that while Cu surfaces can stabilize *HCOO* adlayers at coverages (1/4 ML) limited by intermolecular repulsion, HCOOH can still react (or induce reactions of *HCOO*) through binding at the adlayer interstices (□), onto which H* binds much weaker than on uncovered Cu metal surfaces. Such a hypothesis is consistent with DFT-derived enthalpies for dissociative H_2 adsorption that become positive on Cu(111) surfaces saturated with 1/4 ML *HCOO*, in contrast to the negative values calculated for dissociative H_2 adsorption on bare Cu (111) surfaces (+11 vs. -37 kJ mol^{-1} at 1/16 H_2 ML on bare and *HCOO*-saturated Cu(111); Table 3); all fractional coverages are calculated by the number of adsorbate molecules per surface Cu atom. The corresponding binding modes of dissociative H_2 adsorption on bare and *HCOO*-saturated Cu(111) surfaces are shown in Figures 5a and 5b.

HCOOH can bind molecularly at the interstitial sites (□) to form HCOOH□ on *HCOO*-saturated Cu(111) with DFT-derived adsorption enthalpies that are only slightly less negative than on bare Cu(111) (-51 and -45 kJ mol^{-1} at 1/16 ML HCOOH coverage on bare and *HCOO*-saturated Cu(111); Table 3) because repulsive interactions among bound species are partially compensated by strong H-bonding between HCOOH□ and vicinal *HCOO* species. DFT-optimized structures for molecularly bound HCOOH on bare and *HCOO*-saturated Cu(111) surfaces are shown in Figures 5c and 5d. Molecular HCOOH binding energies on bare Cu surfaces are difficult to measure during TPSR experiments because it immediately dissociates to form *HCOO* and H* even at very low temperature (200 K) [4,20]. HCOOH adsorption enthalpies measured during the steady-state reaction reflect those on *HCOO*-saturated Cu (-100 ± 26 kJ mol^{-1}; Table 3).

Table 3. Adsorption enthalpies (in kJ mol^{-1}) of HCOOH, CO, and H_2 on bare and *HCOO*-saturated Cu surfaces from experiments and theory.

	Exp.		DFT[d]	
	Cu[a]	*HCOO*-saturated Cu/SiO_2	Cu(111)	*HCOO*-saturated Cu(111)
Dissociated H_2	-5 ± 6	N.A.	-37	+11
Molecular HCOOH	N.A.	-100 ± 26[b]	-51	-45
Molecular CO	-50	-34 ± 1[c]	-71	-50

[a]Taken from references ([54,55] for H_2 on Cu(110) and [56] for CO on Cu(111)). [b]Obtained from Table 1. [c]Estimated from the measured $K_{CO,b}$ constant (by the regressing of the rate data in Figures 1 and 5 using the functional form of Equation 7) and from the CO adsorption entropy on Cu(111) from literature [57]. [d]Calculated from DFT methods at 1/16 ML coverages of H_2, CO, and HCOOH on bare and *HCOO*-saturated Cu(111) surfaces. Relevant geometries of each binding mode are shown in Figure 5.

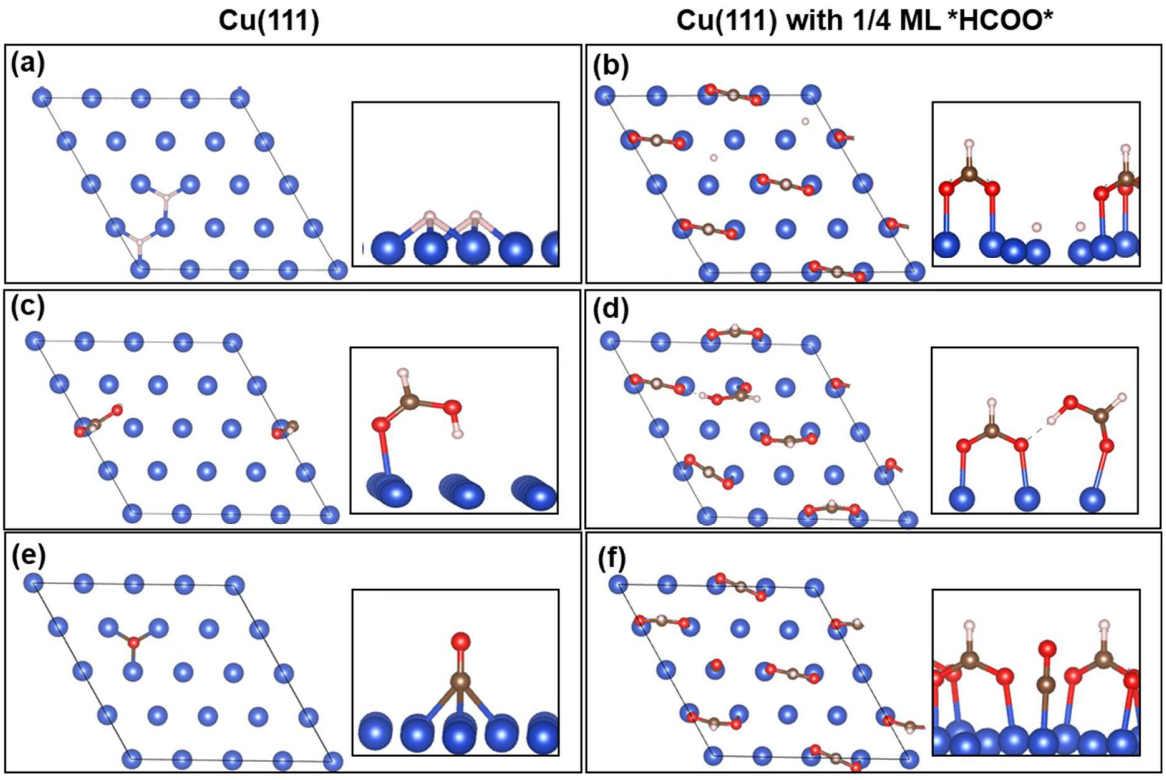

Figure 5. Dissociative H_2 and molecular HCOOH and CO adsorption modes on bare and *HCOO*-saturated Cu(111). These structures were obtained from DFT calculations at 1/16 ML coverages of H_2, CO, and HCOOH on bare and *HCOO*-saturated Cu(111) surfaces.

CO molecules can also bind on such interstices ($CO^{\square}$) within *HCOO* adlayers, as shown by CO infrared bands that persisted on *HCOO*-saturated Cu(100) and decreased in

intensity to 0.3-0.5 of their intensities on bare Cu(100) at 120 K [20]. Consistent with such competitive binding of CO at adlayer interstices, HCOOH dehydrogenation rates decreased with increasing CO pressure (Fig. 6). The assumption of quasi-equilibrated competitive adsorption of CO molecules on □ sites leads to CO_2 formation rates (r_d; per surface Cu atom) given by (derivation in S2; SI):

$$r_d = \frac{k_{app}\, K_{1,b} P_{HCOOH}}{4\left(1 + K_{1,b} P_{HCOOH} + K_{CO,b} P_{CO}\right)} \quad (7)$$

$K_{CO,b}$ represents the equilibrium constant for CO adsorption within the *HCOO* adlayer. The $K_{CO,b}$ constant obtained by regressing the rate data in Figures 1 and 6 to the functional form of Equation 7 is 0.24 ± 0.07 kPa^{-1} at 503 K. This value is about ten-fold smaller than $K_{1,b}$ (1.7 ± 0.6 kPa^{-1} at 503 K), indicative of interstices within *HCOO* adlayer that favor HCOOH□ over CO□. The CO adsorption enthalpy estimated from these measured $K_{CO,b}$ values and CO adsorption entropies on Cu(111) [57] is -34 ± 1 kJ mol^{-1}, which is about 16 kJ mol^{-1} less negative than measured values on clean Cu(111) (-50 kJ mol^{-1} [56]). Such a shift in CO adsorption enthalpy agrees well with DFT-derived energies, which suggest that CO adsorption enthalpies become less negative by 21 kJ mol^{-1} (from -71 to -50 kJ mol^{-1} at 1/16 CO ML; Table 3) when Cu(111) becomes saturated with 1/4 ML *HCOO*; CO binding modes on bare and *HCOO*-saturated Cu(111) are shown in Figures 5e and 5f. This agreement between experimental and theoretical values provides additional confirmation for the presence of a *HCOO* adlayer on Cu surfaces during HCOOH dehydrogenation and for the role of the interstices within such adlayers as the landing sites for catalytic turnovers.

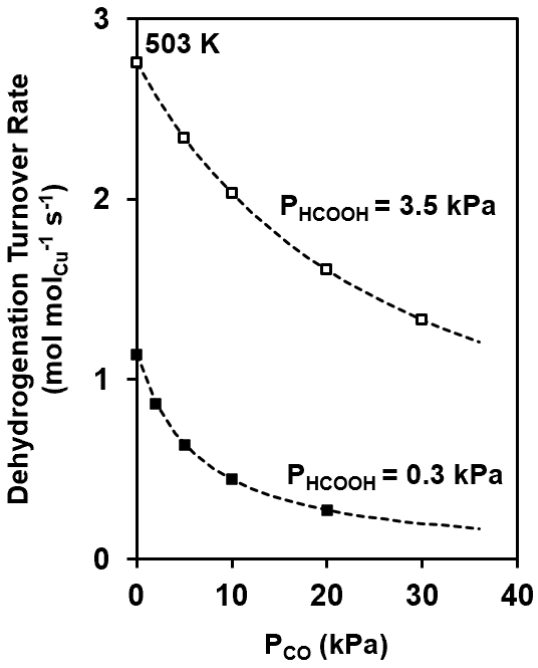

Figure 6. HCOOH dehydrogenation turnover rates on Cu/SiO_2 (5% wt.) as a function of CO pressure (0-30 kPa; 0.3 and 3.5 kPa HCOOH; 503 K). Dashed curves represent the optimal regression of rates using the functional form of Equation 7 (Sec. S3; SI).

DFT-derived enthalpies for dissociative H_2 chemisorption on bare Cu surfaces are much more negative than the measured values (-37 vs. -5 ± 6 kJ mol^{-1} [54,55]; Table 3), an indication that RPBE-D3 functionals overestimate the energies of Cu-H bonds. In contrast, the DFT-derived molecular HCOOH adsorption enthalpies at □ sites within the *HCOO* adlayer are much less negative than the measured value (-45 vs. -100 ± 26 kJ mol^{-1}; Table 3), a consequence of an underestimation of the Cu-O bond strengths. Such methods also tend to overpredict CO binding energies on Cu(111) by overestimating the strength of Cu-C bonds, leading to CO adsorption energies (-76 kJ mol^{-1}; Table 3) that are much more negative than reported experimental values on bare Cu(111) surfaces (-50 kJ mol^{-1} [56]); such inaccuracies of GGA functionals for Cu surfaces cause DFT methods to inaccurately predict stronger binding of CO than HCOOH within the *HCOO* adlayer, in contradiction with experimental trends. These inaccuracies in Cu-C, Cu-O, and Cu-H affinities and the incomplete compensation of these errors among their values leads to DFT-derived mechanistic predictions for Cu-catalyzed HCOOH dehydrogenation, water-gas shift, and methanol synthesis that must remain qualitative [58]. Yet, such errors tend to

cancel out in relative comparisons of energies for the same species on bare and crowded Cu surfaces, leading to accurate assessments of the effects of the *HCOO* adlayer on CO adsorption energies, as shown by the shift in CO adsorption entropies upon saturation of Cu(111) surfaces with 1/4 ML *HCOO* that is accurately described by DFT methods used in this study (16 vs. 21 kJ mol^{-1} from experiment and theory; Table 3). In what follows, we describe infrared spectra that demonstrate the formation of HCOOH□-*HCOO* complexes within the *HCOO* adlayer during HCOOH catalysis and confirm their reactive nature during isothermal surface reactions of pre-adsorbed HCOOH-derived species.

3.3 Infrared spectra during steady-state HCOOH catalysis and isothermal decomposition of pre-adsorbed HCOOH-derived species

Figure 7a depicts illustrative infrared spectra of Cu/SiO_2 samples during HCOOH dehydrogenation (453 K; 3 kPa HCOOH), as well as the evolution of the spectra at 453 K in flowing He after removing HCOOH(g) from the contacting stream. Infrared bands for HCOOH(g) (1790, 1747 cm^{-1}) are detected along with an intense band at 1358 cm^{-1} corresponding to the symmetric O-C-O stretch in *HCOO*; such an assignment was previously reported [19,20] and confirmed here based on DFT-derived vibrational spectra for *HCOO* bound on Cu(111) (at 1/4 ML *HCOO* coverage; red solid spectrum in Fig. 7b; 1300 cm^{-1}). The antisymmetric O-C-O stretch in *HCOO* is not present in the DFT-derived *HCOO* spectrum (red solid spectrum; Fig. 7b) because the dipole moment induced by this vibration lies parallel to the surface and the O-C-O group in *HCOO* is symmetrical with the same C-O distances on the two sides of the C-atom (0.128 nm; Fig. 7). This antisymmetric mode, however, becomes detectable (as a band at 1450 cm^{-1}) when *HCOO* species are adjacent to bound molecular HCOOH (HCOOH□) (blue dashed spectrum; Fig. 7b) because the symmetry of the O-C-O moiety in *HCOO* is perturbed via strong H-bonding with vicinal HCOOH□ species. The C-O bond in *HCOO* is elongated from 0.128 to 0.129 for the O-atom interacting with the H-atom in HCOOH□, while the other C-O bond is shortened (from 0.128 to 0.126 nm; Fig. 7). The DFT-derived spectra for this HCOOH□-*HCOO* complex also include a band at 1650 cm^{-1} that corresponds to the C=O stretch in HCOOH□; this band shifts from 1746 cm^{-1} (for HCOOH(g) from DFT) to 1650 cm^{-1} for the bound HCOOH□ because of interactions between the C=O group in HCOOH□ and the Cu surface (structure shown in Fig. 7).

The infrared spectra measured during steady-state HCOOH catalysis (Fig. 7a) shows features for the symmetric and antisymmetric O-C-O stretches in *HCOO* (1358, 1537 cm^{-1}) and for the C=O stretch in molecular HCOOH□ species (at 1672 cm^{-1}), as expected from the concurrent presence and vicinal nature of HCOOH□ and *HCOO* during HCOOH dehydrogenation turnovers. These bands were also evident upon contacting *HCOO*-saturated Cu(100) surfaces with HCOOH(g) [16].

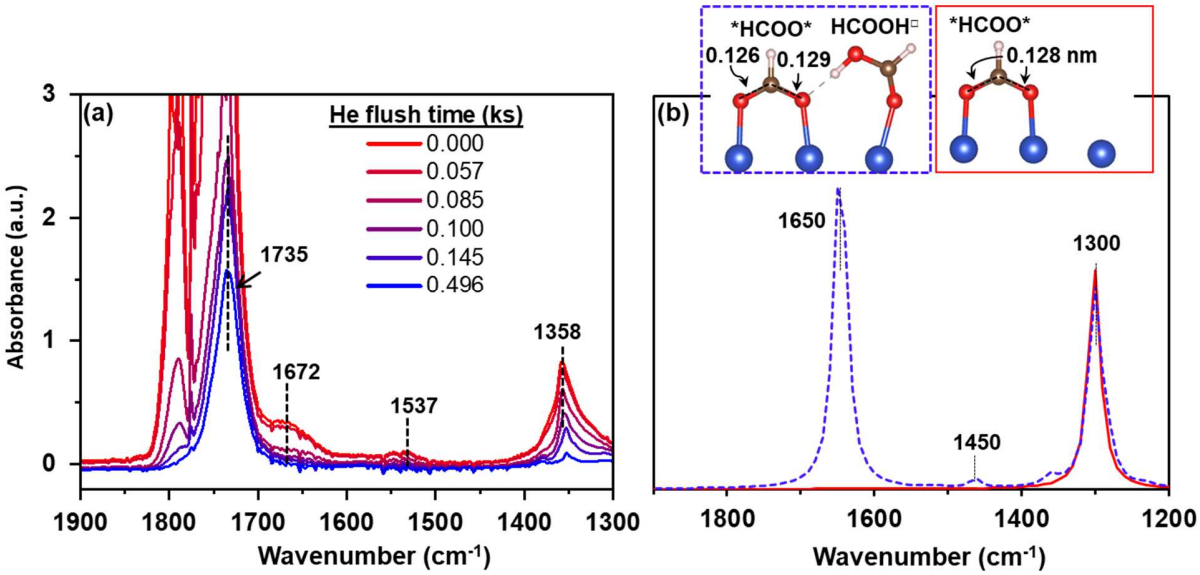

Figure 7. (a) Infrared spectra of Cu/SiO_2 (20% wt.) measured during steady-state HCOOH catalysis (3 kPa HCOOH; 453 K) and in flowing He (at 453 K) after the removal of HCOOH(g) from the reactant stream. The spectrum of Cu/SiO_2 sample measured at 453 K in flowing He before introduction of HCOOH(g) was taken as a reference. (b) DFT-derived infrared spectra of *HCOO*-saturated Cu(111) (at 1/4 ML *HCOO* coverage; red solid spectrum) and a molecularly bound HCOOH□ on *HCOO*-saturated Cu(111) (at 1/16 HCOOH ML; blue dashed spectrum).

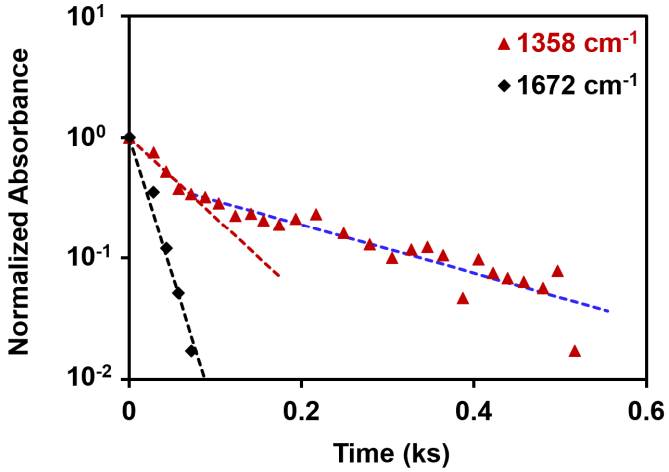

Figure 8. Intensities for infrared bands for *HCOO* (at 1358 cm^{-1}) and HCOOH□ (at 1672 cm^{-1}) on Cu/SiO_2 (20% wt.) as a function of time in flowing He (at 453 K); these values are normalized by their initial values (at t = 0). The spectra are shown in Figure 7. The dashed lines represent the regression of the data to the first-order decomposition (described in Section S5; SI).

The intensities of the infrared bands at 1358 cm^{-1} (for *HCOO*) and 1672 cm^{-1} (for HCOOH□) were monitored at isothermal conditions (453 K) as a function of the time elapsed after the removal of HCOOH(g) (3 kPa) from the flowing He stream (Fig. 8). Such data were regressed by assuming first-order decomposition kinetics, which predict the dashed lines in Figure 8, in order to obtain the first-order rate constants for the disappearance of the *HCOO* and HCOOH□ species. No HCOOH(g) was detected in the effluent, indicating that *HCOO* and HCOOH□ species decomposed before leaving the infrared cell. HCOOH□ species were detected only for the first 0.1 ks after the HCOOH(g) removal from the flowing He stream; the calculated rate constants for the disappearance of HCOOH□ (black dashed line; Fig. 8) and *HCOO* (fitted for < 0.1 ks; red dashed line; Fig. 8) are 53 ± 3 ks^{-1} and 15.2 ± 0.8 ks^{-1}, respectively. As HCOOH□ is depleted (> 0.1 ks), the unimolecular *HCOO* decomposition becomes the only residual route for *HCOO* depletion. The rate constant for unimolecular *HCOO* decomposition, obtained from its band intensities at times beyond 0.1 ks after the complete disappearance of HCOOH□, is 4.6 ± 0.2 ks^{-1} (blue dashed line; Fig. 8). This rate constant is much smaller than those measured for *HCOO* decomposition for the first 0.1 ks when HCOOH□ species co-exist (15.2 ± 0.8 ks^{-1}; red dashed line in Fig. 8) and for HCOOH□ depletion (53 ± 3 ks^{-1}; black dashed line in Fig. 8), indicating that the unimolecular routes occur at significantly lower

rates than their bimolecular counterparts. In the next section, the activation barriers associated with bimolecular decompositions of HCOOH□-*HCOO* complexes and unimolecular *HCOO* decomposition are examined by measuring CO_2 evolution rates and infrared spectra during heating of Cu/SiO_2 samples containing HCOOH-derived species formed through contact with HCOOH(g) at low temperatures.

3.4 Product evolutions and infrared spectra for HCOOH-derived species during temperature ramping (TPSR)

Figure 9 shows CO_2 evolution rates (per surface Cu atom, measured from N_2O titration) and the infrared spectra measured as Cu/SiO_2 samples were heated from 348 to 500 K in flowing H_2 after exposure to 0.5 kPa HCOOH at 348 K; H_2 was used here as the carrier gas in order to remove any spurious O_2 impurities that may deposit chemisorbed O-atom on Cu nanoparticle surfaces. These TPSR profiles were nearly identical, however, with either He or H_2 as the carrier gas (He carrier TPSR shown in Fig. S6, SI). CO_2 and H_2 were the only products formed during heating and neither HCOOH(g) nor CO(g) were detected in the effluent stream.

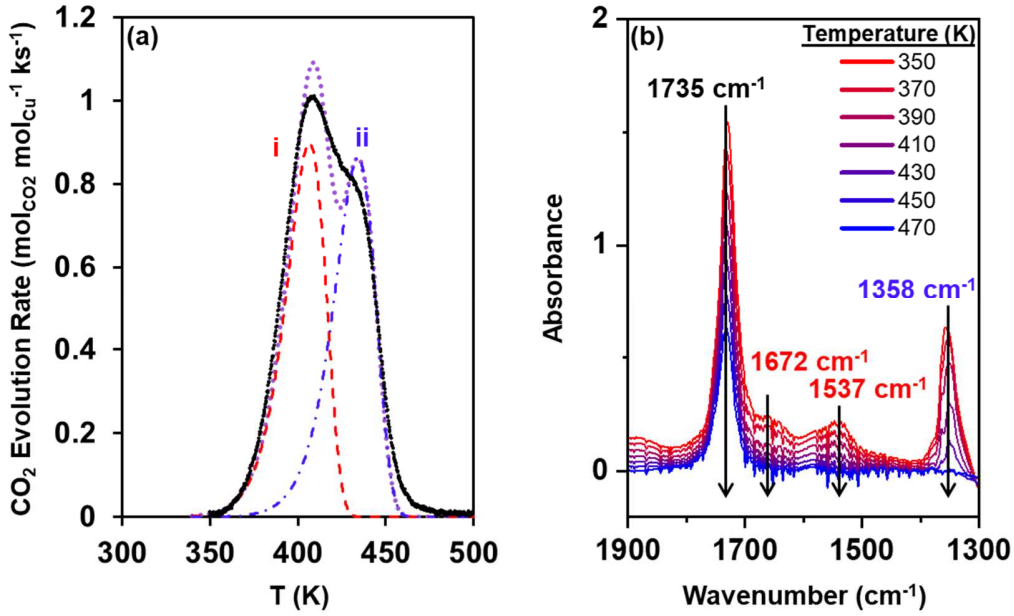

Figure 9. (a) CO_2 evolution rates (per surface Cu atom) and (b) infrared spectra, measured as Cu/SiO_2 (20% wt.) samples were heated from 348 to 500 K (at 0.083 K s^{-1}) in flowing H_2 after exposure to 0.5 kPa HCOOH at 348 K. In the panel (a), The dashed curve (red) and the dashed-dotted curve (blue) reflect the regression of the data assuming the first-order decomposition (Section S6; SI for the fitting details); the dotted curve (purple) represents the sum of the first and second peaks.

CO_2 evolved in two distinct features during heating. The first feature (peak i; Fig. 9a) arises from the desorption of HCOOH(g) from the SiO_2 support and its dehydrogenation via readsorption onto Cu nanoparticle surfaces saturated with *HCOO* adlayers, mediated by the formation and decomposition of HCOOH□-*HCOO* complexes. This conclusion is consistent with the weakening of the HCOOH□ band (at 1672 cm^{-1}) and the perturbed *HCOO* band (at 1537 cm^{-1}) above 350 K and their disappearance above 410 K (Fig. 9b). The presence and desorption of HCOOH bound at SiO_2 surfaces is shown from the 1735 cm^{-1} band, assigned to physisorbed HCOOH on silanols, which weakens as temperature increases from 350 to 500 K (Fig. 9b); the *in situ* infrared spectra measured on SiO_2 (without Cu nanoparticles) are discussed in Section S7 (SI). At higher temperatures, the stranded *HCOO* species decompose via slower unimolecular routes; the symmetric *HCOO* stretch (at 1358 cm^{-1}) weakens with increasing temperature and ultimately disappears above 450 K. The second CO_2 peak (peak ii; Fig. 9a)

coincides with this unimolecular *HCOO* decomposition process and with the disappearance of the *HCOO* stretching mode from the infrared spectrum.

The activation barriers corresponding to the reactions accounting for the first and second features (peaks i and ii; Fig. 9a) are 122 ± 2 and 130 ± 4 kJ mol^{-1}, respectively (Table 4). These barriers were determined by regression of the evolution rates to the functional form predicted by the first-order decomposition kinetics (red dash and blue dashed-dotted curves in Fig. 9a). The activation entropies are nearly zero for both desorption features (Table 4). The barrier for the unimolecular *HCOO* decomposition (peak ii; Fig. 9a; 130 ± 4 kJ mol^{-1}) agrees well with previously reported values, measured by heating Cu(110) (133 kJ mol^{-1} [18]) and Cu/SiO_2 (133 kJ mol^{-1} [16]) containing pre-adsorbed *HCOO* species, and bulk copper formate (125 kJ mol^{-1} [16]). The number of CO_2 molecules evolved in peak ii corresponds to a $CO_2/Cu_{surface}$ ratio of 0.348 ± 0.005, a value slightly higher than 0.25 that is expected for 1/4 ML *HCOO* saturation coverage. This may reflect the gradual desorption of physisorbed HCOOH on SiO_2 support and its reaction on Cu nanoparticles to form CO_2, as shown from the weakening of the 1735 cm^{-1} band (for physisorbed HCOOH on silanols) at temperatures that overlap with those required for the unimolecular decomposition of *HCOO* (Fig. 9b).

The measured barrier for the bimolecular *HCOO* decomposition routes is slightly smaller (by ~8 kJ mol^{-1}) than for the unimolecular routes, consistent with the observed larger *HCOO* decomposition rate constants when HCOOH□ and *HCOO* co-exist during isothermal transient measurements at 453 K (Section 3.3). DFT-derived enthalpies also indicate that such bimolecular routes impose a smaller barrier than unimolecular routes by 9 kJ mol^{-1} (68 vs. 77 kJ mol^{-1}). Such a preference for bimolecular channels reflects HCOOH□ species in the complex that stabilize the kinetically-relevant C-H activation TS more effectively than the *HCOO* precursor through H-bonding, as discussed in more detail in the next section.

Table 4 compares enthalpic and entropic barriers for the two CO_2 evolution features observed upon heating 5, 10 and 20% wt. Cu/SiO_2 samples in flowing He after their respective exposure to 0.5 kPa HCOOH at 348 K; their CO_2 evolution profiles are shown in Figure S6 (SI). These samples contain Cu nanoparticles with different mean diameters (5.0, 9.8, 12.2 nm, respectively, from N_2O titration). Measured $\Delta H^{\ddagger}$ values for each feature were similar among these three Cu/SiO_2 samples; the barriers for the first one (peak i) were 115-116 kJ mol^{-1} and for

the second one (peak ii) were 123-125 kJ mol^{-1}. Estimated $\Delta S^{\ddagger}$ were nearly zero for both features on all samples. These $\Delta H^{\ddagger}$ and $\Delta S^{\ddagger}$ values on 5.0-12.2 nm Cu particles again indicate that surface structures do not strongly influence binding and reactivity for the relevant intermediates in bimolecular and unimolecular routes within the range of particle sizes used in this study. The higher SiO_2/Cu ratios in samples with lower Cu contents (5, 10% wt.) led to the overlapping of two CO_2 evolution features that are more difficult to deconvolute (Fig. S6; SI). This reflects a larger contribution from bimolecular pathways mediated by HCOOH(g) molecules that desorb from SiO_2.

Table 4. Enthalpic and entropic barriers ($\Delta H^{\ddagger}$ and $\Delta S^{\ddagger}$) corresponding to the first and second CO_2 evolution features (peaks i and ii).

Cu/SiO_2	Carrier Gas	$\Delta H^{\ddagger}$ (kJ mol^{-1})		$\Delta S^{\ddagger}$ (J mol^{-1} K^{-1})	
		I	II	I	II
5% wt.[a]	He	115 ± 3	123 ± 10	0 ± 7	0 ± 24
10% wt.[a]	He	116 ± 3	124 ± 10	0 ± 8	0 ± 23
20% wt.[a]	He	115 ± 2	125 ± 6	0 ± 5	0 ± 15
20% wt.[b]	H_2	122 ± 2	130 ± 4	2 ± 5	0 ± 9

Errors reflect the 95% confidence interval. Regression and deconvolution procedure detailed in Section S6 (SI). CO_2 evolution profiles shown in [a]Figure S6 (SI) and [b]Figure 9a.

3.5 Theoretical assessment of HCOOH dehydrogenation via unimolecular and bimolecular routes

This section examines the elementary steps involved in unimolecular and bimolecular decomposition channels through the estimation of the Gibbs free energies of intermediates and transition states using DFT methods (503 K; 1 bar HCOOH).

3.5.1 Elementary steps in unimolecular *HCOO* decomposition

Figure 10 shows DFT-derived Gibbs free energies for intermediates and transition states involved in unimolecular routes mediated by the elementary steps depicted in Scheme 1 (at 1/16 HCOOH ML on Cu(111)). HCOOH binds molecularly on Cu(111) through the O-atom in its C=O group and the H-atom in its O-H group (Fig. 10a) (step 1; Scheme 1); the *HCOOH*

formation free energy is +12 kJ mol^{-1}. *HCOOH* cleaves its O-H bond to form bidentate *HCOO* species interacting with two vicinal Cu surface atoms (*HCOO*; Fig. 10c) and a chemisorbed H-atom (H*; Fig. 10c) (step 2; Scheme 1); the reaction free energy for this step is -23 kJ mol^{-1} and this step is mediated by an O-H activation TS (Fig. 10b) with an activation free energy barrier of +55 kJ mol^{-1}. DFT-derived free energy for the formation of *HCOO* and H* from HCOOH(g) is small and negative (-11 kJ mol^{-1}); this value would lead to an expectation that only ~ 0.01 fraction of the Cu surface would be covered with *HCOO* at 0.1 kPa HCOOH (503 K). Such a prediction contradicts the presence of *HCOO* at saturation coverage on Cu surfaces at all conditions, evidenced by spectroscopic, transient, and kinetic analyses discussed thus far. This discrepancy, in turn, reflects the underestimation of Cu-O bonds strengths by DFT methods (RPBE-D3), as discussed earlier. The remaining *HCOO* moiety (Fig. 10c) reacts via the formation of weakly-bound CO_2 and a bound H-atom (Fig. 10e) in an exergonic step (-22 kJ mol^{-1}) (step 3; Scheme 1); this step is mediated by a C-H activation TS (Fig. 10d) with an activation free energy barrier of 76 kJ mol^{-1}. The weakly-bound CO_2 desorbs in a subsequent exergonic step (-8 kJ mol^{-1}). The remaining two H* can recombine in an exergonic step (-5 kJ mol^{-1}) with an activation free energy barrier of 72 kJ mol^{-1}; the resulting weakly bound H_2 then desorbs in the next step (-23 kJ mol^{-1}) (step 4; Scheme 1), closing the catalytic cycle.

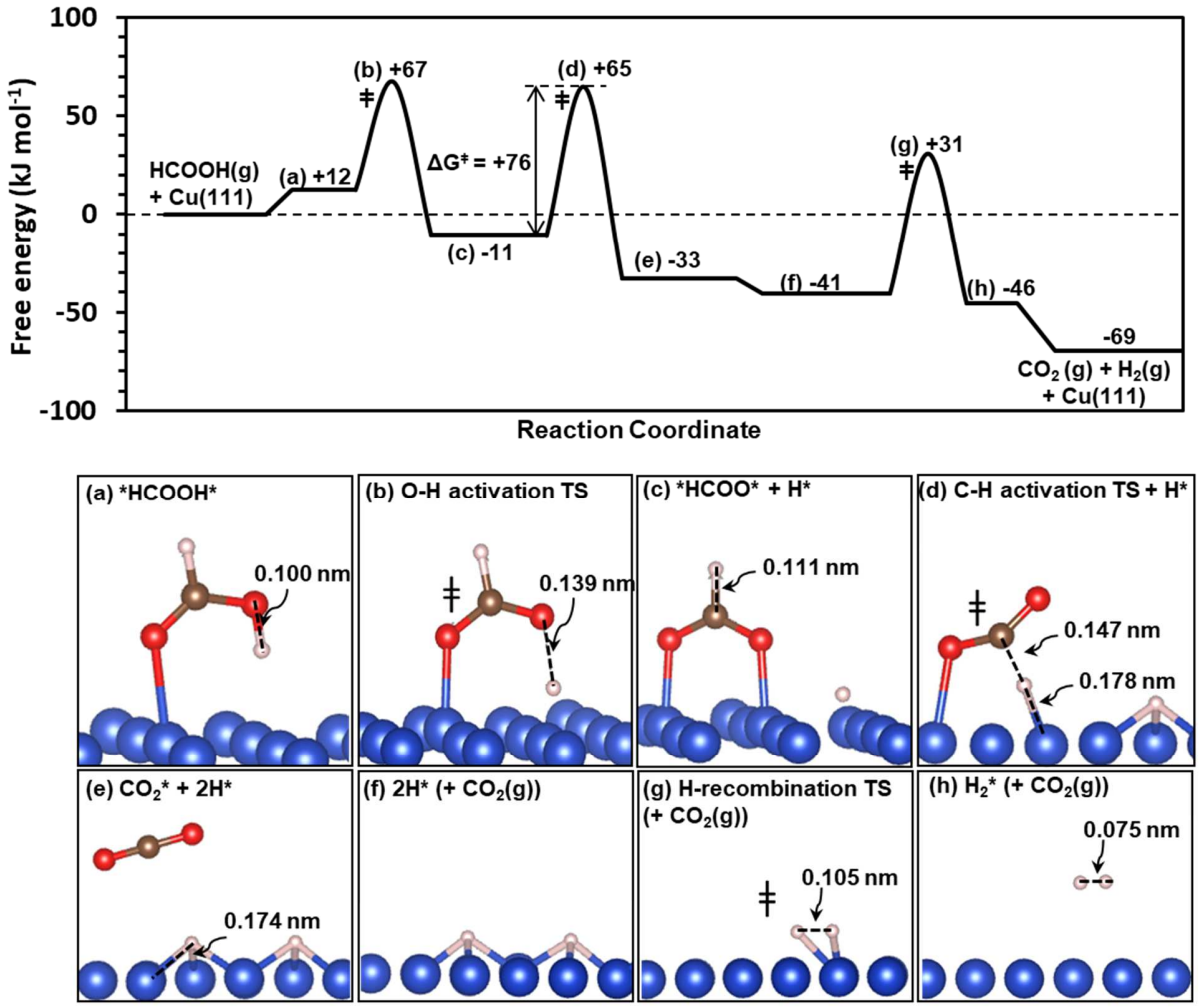

Figure 10. DFT-derived free energies (kJ mol^{-1}; 503 K; 1 bar HCOOH; at 1/16 ML HCOOH coverage on Cu(111)) and structures of intermediates and transition states involved in unimolecular HCOOH dehydrogenation via elementary steps shown in Scheme 1.

The DFT-derived free energies shown in Figure 10 indicate that *HCOO* decomposition barriers to form a CO_2 product (step 3; Scheme 1) are similar to those for the reaction of H* with *HCOO* to re-form *HCOOH* (reverse step 2; Scheme 1) (76 vs. 78 kJ mol^{-1}). These barriers would then lead to a conclusion that the forward rate of *HCOO* decomposition is similar to that of its recombination with H* to re-form *HCOOH*, in which case, the C-H activation in *HCOO* no longer acts as a sole kinetically-relevant step in Scheme 1. These results are inconsistent with previous transient experiments that showed the C-H activation in *HCOO* as the sole kinetically-relevant step for unimolecular HCOOH

decomposition, evidenced by similar CO_2 and H_2 evolution profiles measured from HCOOD and HCOOH [4]; in contrast, CO_2 evolution profiles shifted to higher temperature for *DCOO* than for *HCOO* [17,18]. This discrepancy again seems to reflect the underestimation of Cu-O bonds with RPBE-D3 methods that is not fully compensated when comparing the energies of two TS structures; such errors influence the energies of O-H activation TS more than that of the C-H activation TS, because the former one involves two Cu-O bonds (one fully formed and one partially formed; Fig. 10b), while the later one involves only one Cu-O bond (fully formed; Fig. 10d). Activation free energies include enthalpic and entropic components. DFT-derived activation enthalpy and entropy values for the kinetically-relevant C-H activation step for the unimolecular *HCOO* decomposition (step 3; Scheme 1) are listed in Table 5, along with those measured during transient experiments (peak ii; Fig. 9a) when HCOOH(g) is absent in the reactant stream; the barriers measured during steady-state catalysis reflect those for the bimolecular routes due to the co-presence of weakly-bound HCOOH□ species along with *HCOO*. DFT-derived activation enthalpies for the formation of the C-H activation TS from the *HCOO* precursor ($\Delta H^{\ddagger}_m$ for step 3; Scheme 1) is 77 kJ mol^{-1} (Table 5). This value is much smaller than measured barriers on Cu/SiO_2 (130 ± 4 kJ mol^{-1}) and those reported previously on Cu(110) (133 kJ mol^{-1} [18]) and Cu/SiO_2 (133 kJ mol^{-1} [16]) containing pre-adsorbed *HCOO* species, and bulk copper formate (125 kJ mol^{-1} [16]) (Table 5).

The TS involved in the unimolecular C-H activation step contains a partially-cleaved C-H bond in *HCOO* (0.147 nm at TS; 0.111 nm in *HCOO*; Figs. 10c and 10d) and a Cu-H bond that is nearly-formed (0.178 nm at TS; 0.174 nm in the H* product; Figs. 10d and 10e). Concurrently, one of the Cu-O bonds in *HCOO* is fully cleaved to form a monodentate structure, so as to allow the H-atom in its C-H group to contact the Cu surface (Fig. 10d). The discrepancy between DFT-derived activation barrier and experimental values appears to reflect the tendency of the GGA functionals (RPBE-D3) to significantly underestimate the Cu-O binding, which influences bidentate *HCOO* species more significantly than the monodentate. In contrast, theory-derived activation entropies (+3 J mol^{-1} K^{-1}; Table 5) agree well with near zero experimental values (~ 0 J mol^{-1} K^{-1} for Cu/SiO_2; +30 J mol^{-1} K^{-1} for Cu(110) [4]**;** +16 J mol^{-1} K^{-1} for Cu/SiO_2 [12]**;** Table 5). These small activation entropies, in turn, reflect the immobile nature of the C-H activation TS and its *HCOO* precursor.

DFT-derived Gibbs free energies calculated with PW91 functionals are shown in Figure S8 (discussion in SI), which provide better agreement with experimental observations; these energies indicate that the TS mediating C-H activation in *HCOO* imposes the highest energy barrier along the HCOOH dehydrogenation reaction coordinate. DFT-derived activation enthalpies for the formation of the C-H activation TS from the *HCOO* precursor ($\Delta H^{\ddagger}_{m}$ for step 3; Scheme 1) calculated with PW91 is 88 kJ mol^{-1}, which is closer to the experimental value of 130 ± 4 kJ mol^{-1} (Table 5) compared to the value derived with RPBE-D3 methods (77 kJ mol^{-1}; Table 5). However, these PW91 functionals bring forth other concerns: (i) they predict that HCOOH dissociation to *HCOO* and H* is thermodynamically unfavorable (+5 kJ mol^{-1}; Fig. S8c), contradicting the experimental observation that shows that Cu surfaces are saturated with *HCOO* at all conditions (0.1-3.5 kPa HCOOH; 493-503 K). (ii) In addition, dispersion corrections cannot be currently implemented, to our knowledge, in PW91 calculations; such dispersion corrections are critical to assess bimolecular routes because of the profound effects of long-range van der Waals interactions throughout extended regions of the surface and the critical role of weakly-bound species stabilized by such interactions. As a result, we only tested RPBE-D3 methods in assessing energies of intermediates and transition states for bimolecular routes, which we discuss in the next section.

Table 5. Activation enthalpy and entropy barriers for unimolecular *HCOO* decomposition route from experiment and theory.

			$\Delta H^{\ddagger}_{m}$ (kJ mol^{-1})	$\Delta S^{\ddagger}_{m}$ (J mol^{-1} K^{-1})
Experiments		Cu/SiO_2 [a]	130 ± 4	0 ± 9
		Cu(110) [b]	133	+30[d]
		Cu/SiO_2 [c]	133	+16[d]
		Bulk Copper formate [c]	125	N/A
Theory	RPBE-D3	Cu(111)[e]	77	+3
	PW91		88	+2

[a]This work for 20% wt. Cu/SiO_2 with H_2 as a carrier gas (Table 4). [b]Madix and Telford [18] [c]Iglesia and Boudart [12] [d]Values estimated based on transition-state theory formalism with temperatures of [a]450 K and [b]453.6 K. [e]DFT calculations were performed at 1/16 ML coverage. Geometries of intermediates and transition states are shown in Figure 10.

3.5.2 Elementary steps in bimolecular decomposition of HCOOH□-*HCOO* complexes

This section describes DFT-based assessments of the bimolecular HCOOH dehydrogenation routes mediated by the decomposition of HCOOH□-*HCOO* complexes.

Infrared spectra measured during HCOOH catalysis show that *HCOO* and HCOOH□ species co-exist during HCOOH dehydrogenation on Cu nanoparticles (Section 3.3). Such HCOOH□-*HCOO* complexes can decompose bimolecularly with activation barriers lower than those for unimolecular *HCOO* decomposition (Sections 3.3 and 3.4). HCOOH□-*HCOO* pairs can form CO_2 via reactions of either the HCOOH□ or the *HCOO* species in the pair; the respective elementary steps for these two paths are depicted in Schemes 2a and 2b. These two routes can be discerned using DFT-derived free energies of relevant intermediates and transition states, but they cannot be distinguished experimentally.

Figure 11 shows the Gibbs free energies (503 K; 1 bar HCOOH) of the intermediates and transition states involved in the decomposition of the HCOOH□ in HCOOH□-*HCOO* complexes (via the elementary steps in Scheme 2a); the energies are calculated at 1/16 HCOOH ML (one HCOOH per 16 surface Cu atoms) on *HCOO*-saturated Cu(111) (with 4 *HCOO* per 16 Cu atoms). The energies of HCOOH adsorption on interstitial sites, however, remained similar (within 1 kJ mol^{-1}), when the HCOOH□ coverage increased from 1/16 ML to 1/8 ML on *HCOO*-saturated surfaces, indicating minimal interactions among bound HCOOH□ species within the interstitial sites.

HCOOH(g) binds molecularly on an interstitial site (□) of *HCOO*-saturated Cu(111) to form a HCOOH□-*HCOO* complex (Figs. 11a and 11a'). HCOOH□ in the complex can interact with the surface through its O-atom in either the C=O group (Fig. 11a) or the OH group (Fig. 11a'), with the former configuration being slightly more favorable (by 3 kJ mol^{-1}) based on DFT-derived energies (Fig. 11). Such a conclusion is consistent with measured infrared bands that show the shift in the C=O stretching mode from 1747 cm^{-1} (for HCOOH(g)) to 1672 cm^{-1} for the bound HCOOH□ (Fig. 7a), indicating strong interactions between the C=O group in HCOOH□ and the Cu surface (Section 3.3). The free energy change for this step ($\Delta G_{1,b}$; step 1; Scheme 2) determines the $K_{1,b}$ constant (in Eq. 4) via Equation 5. The $\Delta G_{1,b}$ value from DFT methods is positive (+35 kJ mol^{-1}; 503 K), in contrast with the negative values (-21 kJ mol^{-1}) determined from measured $K_{1,b}$ values (Table 1). These discrepancies again reflect underestimates of the strength of the Cu-O bond formed upon molecular HCOOH adsorption on the interstitial sites to form HCOOH□ (Fig. 11a), which is also reflected in the reaction enthalpy for this step (-45 kJ mol^{-1}; Table 1) that is much less negative than the measured value (-100 ± 26 kJ mol^{-1}; Table 1).

In contrast, the theory-derived reaction entropy for this HCOOH□ formation step (step 1; Scheme 2) (-160 J mol^{-1} K^{-1}; Table 1) agrees well with the experimental value (-160 ± 53 J mol^{-1} K^{-1}; Table 1).

The HCOOH□ species in the *HCOO* adlayer interstices (Fig. 11a) can decompose to form a CO_2 product via the elementary steps shown in Scheme 2a. In this route, HCOOH□ reorients itself and reacts with the interstitial Cu site (□) to cleave its C-H bond, as the vicinal *HCOO* abstracts the H-atom in HCOOH□ and cleaves the O-H bond in HCOOH□. This kinetically-relevant concerted C-H and O-H activation step forms a weakly-bound CO_2□ and H□ at the Cu surface, along with the *HCOOH* that formed upon H-abstraction by *HCOO* (Fig. 11c); the free energy change for this step is -36 kJ mol^{-1}. This C-H and O-H activation occurs in a nearly concerted manner and the sequential activation transition states could not be located using DFT methods. The free energy barrier for the formation of this C-H and O-H activation TS from the HCOOH□-*HCOO* complex is 86 kJ mol^{-1} (Fig. 11b). The weakly bound CO_2□ formed subsequently desorbs in the exergonic step (-35 kJ mol^{-1}; Fig. 11d). The *HCOOH* left at the surface then cleaves its O-H bond via a H□-assisted pathway to re-form *HCOO* and a weakly-bound H_2□ (Fig. 11f); this step is slightly endergonic with a reaction energy of +3 kJ mol^{-1} and involves a H_2-recombination TS (Fig. 11e) with an activation free energy barrier of 80 kJ mol^{-1}. The H_2□ formed then desorbs in an exergonic step (-36 kJ mol^{-1}) to reform □ sites and close the catalytic cycle.

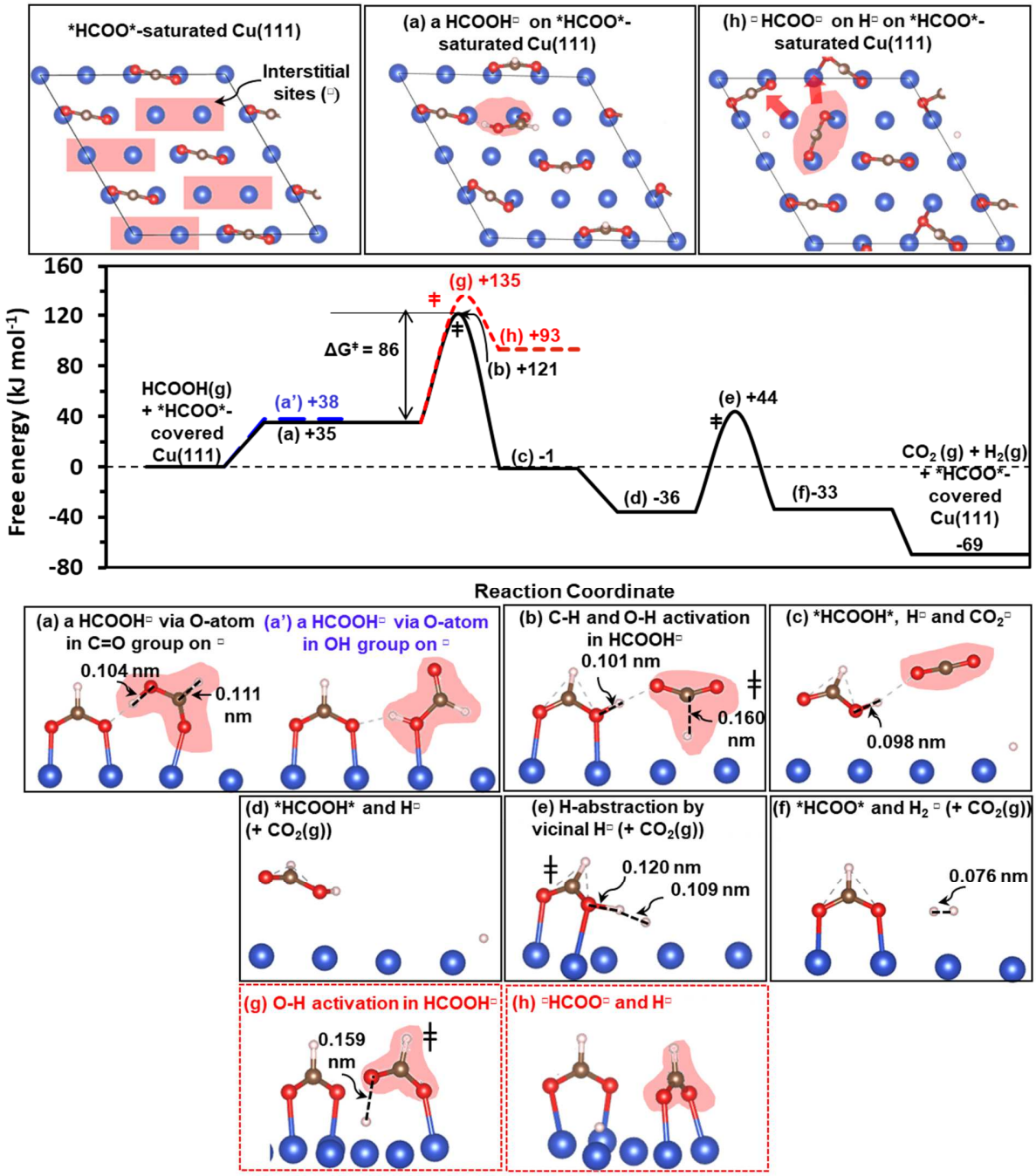

Figure 11. DFT-derived free energies (kJ mol^{-1}; 503 K; 1 bar HCOOH) and structures of intermediates and transition states involved in the bimolecular HCOOH dehydrogenation route via elementary steps in Scheme 2a. These calculations are performed at 1/6 ML HCOOH coverage on *HCOO*-saturated Cu(111).

The TS that mediates the concerted C-H and O-H activation (Fig. 11b) imposes the highest free energy barrier along the reaction coordinate for HCOOH□ decomposition (Fig. 11).

This TS contains a C-H bond that is partially cleaved (0.111 nm in HCOOH□; 0.160 nm in TS; Figs. 11a and 11b). In contrast, the O-H bond at this TS is already nearly-formed (0.101 nm in TS; 0.098 nm in *HCOOH* products; Figs. 11b and 11c). As a result, DFT-derived KIE values, defined as the ratios of $k_{d,b}$ for different isotopologues, are larger than unity and similar for HCOOH/DCOOH and HCOOH/DCOOD (2.6 and 2.4, respectively). These KIE values agree well with the measured values of 2.2 ± 0.2 for HCOOH/DCOOH and 2.4 ± 0.2 for HCOOH/DCOOD (Table 3).

The molecularly-bound HCOOH□ moiety in HCOOH□-*HCOO* complexes (Fig. 11a) may instead cleave its O-H bond by reacting with exposed Cu atoms at the interstitial sites (□) to form another bidentate formate (□HCOO□) and a chemisorbed H-atom (H□) (Fig. 11h). This step, however, involves a large free energy barrier (100 kJ mol^{-1}; Fig. 11g). This barrier is much larger than that for the HCOOH□ decomposition (86 kJ mol^{-1}; Fig. 11b) or the *HCOO* decomposition (59 kJ mol^{-1}; Fig. 12, discussed next) in HCOOH□-*HCOO* complexes. CO_2 formation via *HCOO* decomposition in HCOOH□-*HCOO* complexes is thus much more facile than □HCOO□ formation. This □HCOO□ and H□ formation step is also very endergonic (+58 kJ mol^{-1}) because the □HCOO□ formed at the interstitial sites (□) experiences repulsive interactions within the *HCOO* adlayer; *HCOO* species in the *HCOO* adlayer become disordered in order to maximize their distances from □HCOO□ (Fig. 11h). These results, in turn, provide theoretical evidence that the surface coverages of *HCOO* species saturate at 1/4 ML *HCOO*.

Figure 12 shows the free energies of the intermediates and transition states involved in the alternative HCOOH□-*HCOO* decomposition pathway depicted in Scheme 2b. In this route, the *HCOO* moiety in the HCOOH□-*HCOO* complex cleaves one of its two Cu-O bonds to form a monodentate formate (HCOO*; Fig. 12b) that is stabilized by H-bonding with the vicinal HCOOH□ in the complex; this step is endergonic (+15 kJ mol^{-1}) but is required for the *HCOO* species to react with the surface Cu atom in the next step. The Cu atom (*) freed by the formation of monodentate HCOO* from bidentate *HCOO* then abstracts a H-atom from HCOO* via a C-H activation TS stabilized by H-bonding with the vicinal HCOOH□ (Fig. 12c). This C-H activation in *HCOO* forms weakly-bound CO_2* and H* species at the Cu surface (Fig. 12d); the free energy change for this step is -26 kJ mol^{-1}. CO_2 desorbs and the remaining HCOOH□ can reorient itself to interact with the surface in an exergonic step (-42 kJ mol^{-1}; Fig. 12e) to re-form *HCOO* through an O-H activation step involving either a Cu surface atom (TS

in Fig. 12f') or a H* (TS in Fig. 12f), thus completing a catalytic turnover. DFT-derived energies show that the later route (the H*-assisted O-H activation in HCOOH□) occurs at a much lower

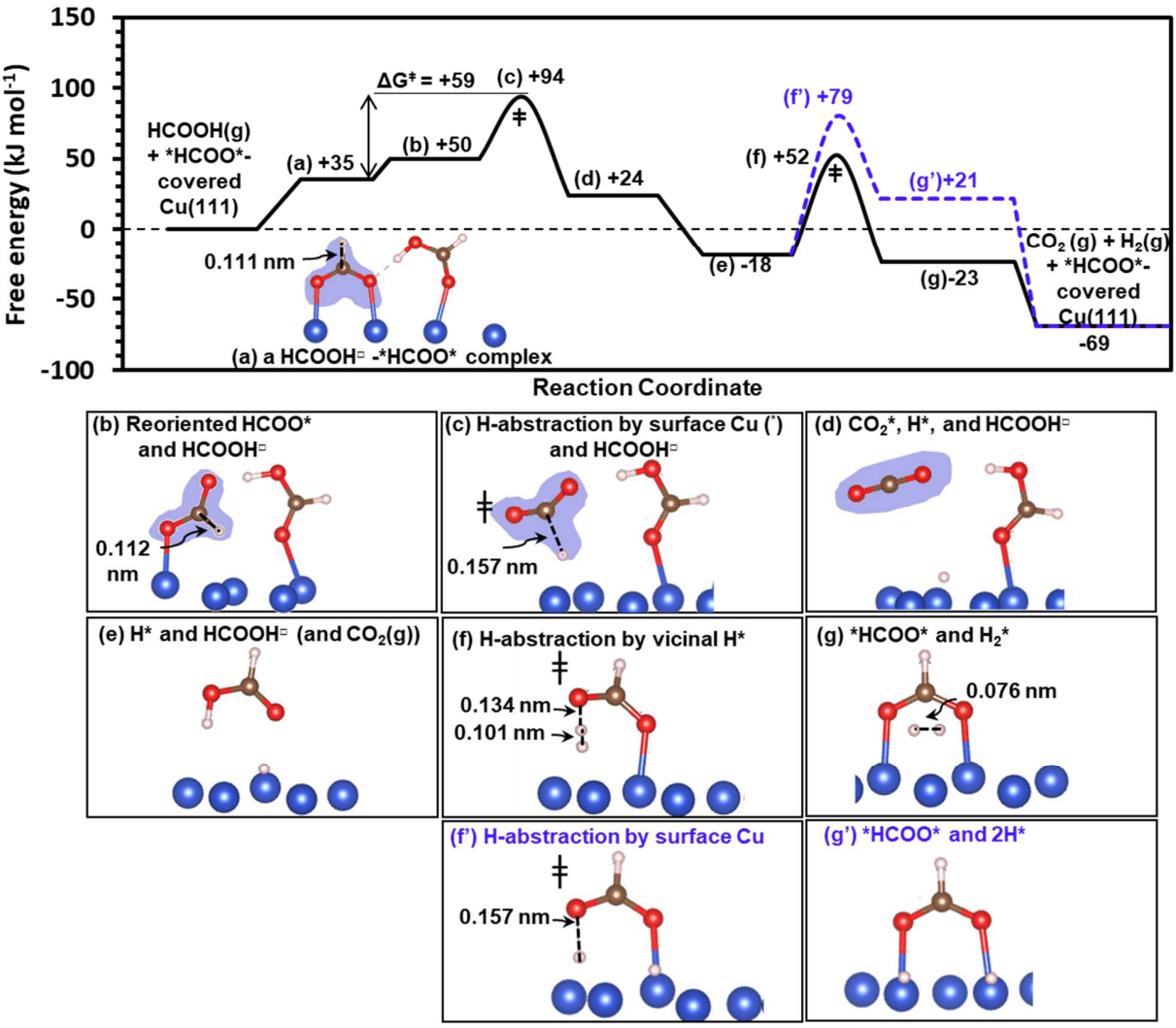

activation free energy barrier than the former route (70 vs. 97 kJ mol^{-1}).

Figure 12. DFT-derived free energies (kJ mol^{-1}; 503 K; 1 bar HCOOH) and structures of intermediates and transition states involved in the bimolecular HCOOH dehydrogenation route via elementary steps in Scheme 2b. These calculations are performed at 1/6 ML HCOOH coverage on *HCOO*-saturated Cu(111).

The TS that mediates C-H activation in monodentate HCOO* in this *HCOO* decomposition route exhibits the highest free energy along the reaction coordinate. The C-H bond in HCOO* is partially cleaved at the TS (0.111 nm in *HCOO*; 0.157 nm in the TS; Figs.

12a, 12c). DFT-derived KIE values, taken as the $k_{d,b}$' constant ratios for HCOOH/DCOOH and HCOOH/DCOOD, are 2.4 and 2.1, respectively, which also agree well with experimental values (2.2 ± 0.2 for HCOOH/DCOOH and 2.4 ± 0.2 for HCOOH/DCOOD; Table 3). Thus, KIE values cannot distinguish whether HCOOH□ or *HCOO* species predominantly decompose in the HCOOH□-*HCOO* complexes (Schemes 2a and 2b). DFT-derived free energies suggest, however, that *HCOO* decomposition routes proceed with a much lower free energy barrier (59 kJ mol^{-1}; Fig. 12) than HCOOH□-decomposition pathways (86 kJ mol^{-1}; Fig. 11) (both barriers are referenced to their common HCOOH□-*HCOO* precursor complex). The ratio of rate constants for HCOOH□ and *HCOO* decomposition routes ($k_{d,b}/k_{d,b}$'), estimated from these barriers at 503 K, is ~ 0.002, indicating that the decomposition of *HCOO* in the complex occurs at much faster rates than HCOOH□ decomposition; the measured k_{app} constants thus primarily reflect the $k_{d,b}$' constants for bimolecular *HCOO* decomposition pathway.

The DFT-derived free energy barrier for this preferred bimolecular *HCOO* decomposition route (59 kJ mol^{-1}; Fig. 12) is also smaller than that for the unimolecular decomposition routes (76 kJ mol^{-1}; Fig. 10), as a result of the preferential H-bonding stabilization of the C-H activation TS over the *HCOO* precursors by vicinal HCOOH□ species. These intermolecular interactions are also evident in enthalpic barriers that are 11 kJ mol^{-1} smaller for bimolecular routes (68 vs. 79 kJ mol^{-1} for unimolecular *HCOO* routes). These conclusions are consistent with activation barriers for the bimolecular routes derived from TPSR data (peak i; Fig. 9a) that are 8 kJ mol^{-1} lower than for unimolecular routes (peak ii; Fig. 9a) (122 ± 2 vs 130. ± 4 kJ mol^{-1}; Table 4; 20% wt. Cu/SiO_2). Moreover, these results show that inaccurate DFT assessments of Cu-O and Cu-H bond energies tend to cancel when examining differences in activation barriers between unimolecular and bimolecular routes despite the absolute values of such barriers lacking quantitative agreements with experimental measurements.

Results from kinetic, isotopic, spectroscopic, and transient experiments and DFT calculations discussed thus far provide compelling evidence that Cu surfaces are saturated with *HCOO* species that present at their saturation 1/4 ML coverages at all relevant conditions (0.1-3.5 kPa HCOOH; 473-503 K). HCOOH dehydrogenation catalysis on *HCOO* saturated Cu surfaces occurs via bimolecular reactions between HCOOH□, adsorbed within the interstitial sites within the *HCOO* adlayer, and *HCOO*, which, in turn, open reaction channels for

HCOOH to react with lower activation barriers than for the unimolecular *HCOO* decomposition. We thus surmise that bimolecular routes are responsible for HCOOH dehydrogenation rates measured during steady-state catalysis. Such a conclusion is in sharp contrast to a recent theoretical study, which suggested the involvement of both unimolecular and bimolecular routes during HCOOH catalysis [27]. Specifically, this study, based on DFT calculations and microkinetic modeling, suggested that the unimolecular routes account for nearly 50% of overall turnover rates at 10 kPa HCOOH and 385 K. By such evidence and treatments, the conditions of our experiments at lower pressures and higher temperatures (0.1-3.5 kPa HCOOH; 473-503 K) would result in the nearly exclusive involvement of unimolecular routes, in sharp contradiction to our results and conclusions based on experimental methods benchmarked against theory. Such differences may have been caused by using different surface models in their DFT calculations (e.g., calculating energies on Cu(111) surfaces with 3/16 ML *HCOO* and an equal number of co-adsorbed HCOOH*, opposed to our calculations with 1/4 ML *HCOO* saturation coverages) and/or by problems of GGA functionals in accurately predicting the energies of intermediates and transition states on Cu surfaces.

4. Conclusion

This work combines kinetic, isotopic, spectroscopic, and transient experiments with DFT calculations to assess the mechanistic details of HCOOH dehydrogenation on Cu nanoparticles. HCOOH decomposes selectively to its dehydrogenation products (CO_2 and H_2) without any detectable formation of dehydration products (CO_2 and H_2O). Cu surfaces are saturated with *HCOO* species at all practical conditions (0.1-3.5 kPa HCOOH; 473-503 K), which reach their saturation at 1/4 ML *HCOO* coverages due to the repulsive interactions among bound formate species. HCOOH can instead bind molecularly at interstitial sites (□) on *HCOO*-saturated Cu surfaces and form HCOOH□-*HCOO* complexes, where their co-existence and vicinal nature are evident from *in situ* infrared spectra. These weakly-bound HCOOH□ species promote the decomposition of the vicinal *HCOO* by stabilizing the C-H activation TS more effectively than it stabilizes the *HCOO* precursor via H-bonding, as we show from DFT-derived energies and confirm with TPSR measurements.

Bimolecular *HCOO* decomposition routes discussed in this work are consistent with all experimental and theoretical observations. Such routes are less relevant at low *HCOO*

coverages prevalent in reactions of pre-formed bound species and in model systems typically treated by theoretical methods. The presence of gaseous HCOOH reactants and high *HCOO* coverages during steady-state catalysis, however, open reaction channels unavailable during stoichiometric reactions of bound species present at low coverages, allowing the reactions of strongly bound *HCOO* at much lower barriers. The results of this work, in turn, present yet another example showing how crowded surfaces can facilitate catalysis by selectively stabilizing the relevant TS more so than the precursor through interactions with more weakly bound species.

Personal Acknowledgement

A method of analysis, clarity of thought, and a penchant for rigor remain the enduring legacy of Michel Boudart. It is our joint intent, as members of his academic progeny, to honor his memory with this contribution about a topic that he found of keen interest. In those instances when showmanship replaces scholarship, Michel reminds us of our purpose as guardians of rigor and as teachers of catalysis, with his career and example as a beacon shining bright. He dedicated his professional life to the creation of "recyclable knowledge" and to mentoring generations of students and we are asked today to pass on the torch. Those among us fortunate to have known Michel well (directly or indirectly) are different and better because of his touch, a touch made softer by his inseparable lifelong companion, Marina Boudart.

Acknowledgement

The authors thank Prof. Prashant Deshlahra at Tufts University for providing a computational tool to generate DFT-derived infrared spectra. We also thank Michelle Nolen at Colorado School of Mines for carefully proofreading our manuscript. UDLT acknowledges the financial support from the European Union's Horizon 2020 research and innovation program under the Marie Skłodowska-Curie grant (agreement number 891636). SK thanks the startup funding support from Colorado School of Mines. This work is supported by the U.S. Department of Energy, Office of Science, Office of Basic Energy Sciences (Contract No. DE-AC05-76RL0- 1830). This research was accomplished by using computing resources from the National Energy Research Scientific Computing Center (NERSC), a DOE Office of Science User Facility supported by the Office of Science of the U.S. Department of Energy (Contract No. DE-AC02-05CH11231).

References

[1] M. Grasemann, G. Laurenczy, Formic acid as a hydrogen source – recent developments and future trends, Energy Environ. Sci. 5 (2012) 8171. doi:10.1039/c2ee21928j.

[2] D.M. Alonso, J.Q. Bond, J.A. Dumesic, Catalytic conversion of biomass to biofuels, Green Chem. 12 (2010) 1493. doi:10.1039/c004654j.

[3] E. Iglesia, M. Boudart, Decomposition of Formic Acid on Copper, Nickel, Alloys, J. Catal. 81 (1983) 214–223.

[4] D.H.S. Ying, R.J. Madix, Thermal desorption study of formic acid decomposition on a clean Cu(110) surface, J. Catal. 61 (1980) 48–56. doi:10.1016/0021-9517(80)90338-3.

[5] F.S. Stone, D. Waller, Cu-ZnO and Cu-ZnO/Al2O3 catalysts for the reverse water-gas shift reaction. The effect of the Cu/Zn ratio on precursor characteristics and on the activity of the derived catalysts, Top. Catal. 22 (2003) 305–318. doi:10.1023/A:1023592407825.

[6] M.S. Spencer, The role of zinc oxide in Cu/ZnO catalysts for methanol synthesis and the water–gas shift reaction, Top. Catal. 8 (1999) 259–266. doi:10.1023/A:1019181715731.

[7] A.A. Gokhale, J.A. Dumesic, M. Mavrikakis, On the mechanism of low-temperature water gas shift reaction on copper, J. Am. Chem. Soc. 130 (2008) 1402–1414. doi:10.1021/ja0768237.

[8] Y. Yang, C.A. Mims, R.S. Disselkamp, D. Mei, J.H. Kwak, J. Szanyi, C.H.F. Peden, C.T. Campbell, Isotope effects in methanol synthesis and the reactivity of copper formates on a Cu/SiO2 catalyst, Catal. Letters. 125 (2008) 201–208. doi:10.1007/s10562-008-9592-4.

[9] Y. Yang, C.A. Mims, D.H. Mei, C.H.F. Peden, C.T. Campbell, Mechanistic studies of methanol synthesis over Cu from CO/CO2/H2/H2O mixtures: The source of C in methanol and the role of water, J. Catal. 298 (2013) 10–17. doi:10.1016/j.jcat.2012.10.028.

[10] G.J. Miller, D. Newton, G.A. Browmaker, R.P. Cooney, In situ FT-IR investigation of formic acid adsorption on reduced and reoxidized copper catalysts, Appl. Spectrosc. 48 (1994) 827–832. doi:10.1366/0003702944029893.

[11] H.S. Inglis, D. Taylor, Decomposition of Formic Acid on Titanium, Vanadium, Chromium, Manganese, Iron, Cobalt, Nickel, and Copper, J Chem Soc Inorg Phys Theor. 19 (1969) 2985–2987.

[12] E. Iglesia, B. Michel, Unimolecular and bimolecular formic acid decomposition on copper, J. Phys. Chem. 20 (1986) 5272–5274. doi:10.1021/j100412a074.

[13] E. Iglesia, M. Boudart, Decomposition of Formic Acid on Copper, Nickel, Alloys II. Catalytic and Temperature-Programmed Decomposition of Formic Acid on Cu/Si02, Cu/A1203, and Cu Powder, J. Catal. 81 (1983) 214–223.

[14] M. Bowker, R.J. Madix, XPS, UPS and thermal desorption studies of the reactions of formaldehyde and formic acid with the Cu(110) surface, Surf. Sci. 102 (1981) 542–565. doi:10.1016/0039-6028(81)90045-5.

[15] M.D. Marcinkowski, C.J. Murphy, M.L. Liriano, N.A. Wasio, F.R. Lucci, E.C.H. Sykes, Microscopic View of the Active Sites for Selective Dehydrogenation of Formic Acid on Cu(111), ACS Catal. 5 (2015) 7371–7378. doi:10.1021/acscatal.5b01994.

[16] E. Iglesia, M. Boudart, Unimolecular and bimolecular formic acid decomposition on copper, J. Phys. Chem. 90 (1986) 5272–5274. doi:10.1021/j100412a074.

[17] Y. Yao, F. Zaera, Adsorption and thermal chemistry of formic acid on clean and oxygen-predosed Cu(110) single-crystal surfaces revisited, Surf. Sci. 646 (2016) 37–44. doi:10.1016/j.susc.2015.06.007.

[18] R.J. Madix, S.G. Telford, The kinetic isotope effect for C-H bond activation on Cu(110): the effects of tunnelling, Surf. Sci. 227 (1992) 246–252. doi:https://doi.org/10.1016/0039-6028(92)90765-X.

[19] M. Bowker, S. Haq, R. Holroyd, P.M. Parlett, S. Poulston, N. Richardson, Spectroscopic and kinetic studies of formic acid adsorption on Cu(110), J. Chem. Soc., Faraday Trans. 92 (1996) 4683–4686.

[20] L.H. Dubois, T.H. Ellis, B.R. Zegarski, S.D. Kevan, New insights into the kinetics of formic acid decomposition on copper surfaces, Surf. Sci. 172 (1986) 385–397. doi:10.1016/0039-6028(86)90763-6.

[21] H. Nakano, I. Nakamura, T. Fujitani, J. Nakamura, Structure-Dependent Kinetics for Synthesis and Decomposition of Formate Species over Cu(111) and Cu(110) Model Catalysts, J. Phys. Chem. B. 105 (2001) 1355–1365. doi:10.1021/jp002644z.

[22] S. Li, J. Scaranto, M. Mavrikakis, On the Structure Sensitivity of Formic Acid Decomposition on Cu Catalysts, Top. Catal. 59 (2016) 1580–1588. doi:10.1007/s11244-016-0672-1.

[23] J.A. Herron, J. Scaranto, P. Ferrin, S. Li, M. Mavrikakis, Trends in Formic Acid Decomposition on Model Transition Metal Surfaces: A Density Functional Theory study, ACS Catal. 4 (2014) 4434–4445. doi:10.1021/cs500737p.

[24] J.S. Yoo, F. Abild-Pedersen, J.K. Nørskov, F. Studt, Theoretical Analysis of Transition-Metal Catalysts for Formic Acid Decomposition, ACS Catal. 4 (2014) 1226–1233. doi:10.1021/cs400664z.

[25] Z. Jiang, P. Qin, T. Fang, Decomposition mechanism of formic acid on Cu (111) surface: A theoretical study, Appl. Surf. Sci. 396 (2016) 857–864. doi:10.1016/j.apsusc.2016.11.042.

[26] B.W.J. Chen, M. Mavrikakis, Formic Acid: A Hydrogen-Bonding Cocatalyst for Formate Decomposition, ACS Catal. 10 (2020) 10812–10825. doi:10.1021/acscatal.0c02902.

[27] B.W.J. Chen, S. Bhandari, M. Mavrikakis, Role of Hydrogen-bonded Bimolecular Formic Acid-Formate Complexes for Formic Acid Decomposition on Copper: A Combined First-Principles and Microkinetic Modeling Study, ACS Catal. 11 (2021) 4349–4361. doi:10.1021/acscatal.0c05695.

[28] S. Kwon, T.C. Lin, E. Iglesia, Elementary steps and site requirements in formic acid

dehydration reactions on anatase and rutile TiO2 surfaces, J. Catal. 383 (2020) 60–76. doi:10.1016/j.jcat.2019.12.043.

[29] J. Liu, D. Hibbitts, E. Iglesia, Dense CO Adlayers as Enablers of CO Hydrogenation Turnovers on Ru Surfaces, (2017). doi:10.1021/jacs.7b04606.

[30] C.J.G. Van Der Grift, P.A. Elberse, A. Mulder, J.W. Geus, Preparation of silica-supported copper catalysts by means of deposition-precipitation, Appl. Catal. 59 (1990) 275–289. doi:10.1016/S0166-9834(00)82204-6.

[31] E. Iglesia, M. Boudart, Decomposition of Formic-Acid on Copper, Nickel, and Copper Nickel-Alloys .1. Preparation and Characterization of Catalysts, J. Catal. 81 (1983) 204–213. doi:10.1016/0021-9517(83)90158-6.

[32] G.C. Chinchen, C.M. Hay, H.D. Vandervell, K.C. Waugh, The measurement of copper surface areas by reactive frontal chromatography, J. Catal. 103 (1987) 79–86. doi:10.1016/0021-9517(87)90094-7.

[33] A. Karelovic, P. Ruiz, The role of copper particle size in low pressure methanol synthesis via CO2 hydrogenation over Cu/ZnO catalysts, Catal. Sci. Technol. 5 (2015) 869–881. doi:10.1039/C4CY00848K.

[34] G.J.J. Bartley, R. Burch, R.J. Chappell, Investigation of the dispersion of supported copper catalysts by oxygen adsorption and nitrous oxide decomposition, Appl. Catal. 43 (1988) 91–104. doi:10.1016/S0166-9834(00)80903-3.

[35] D.R. Stull, Vapor Pressure of Pure Substances. Organic and Inorganic Compounds, Ind. Eng. Chem. 39 (2005) 517–540. doi:10.1021/ie50448a022.

[36] Kresse, Furthmüller, Efficient iterative schemes for ab initio total-energy calculations using a plane-wave basis set., Phys. Rev. B. Condens. Matter. 54 (1996) 11169–11186. doi:10.1103/physrevb.54.11169.

[37] B. Hammer, L. Hansen, J. Nørskov, Improved adsorption energetics within density-functional theory using revised Perdew-Burke-Ernzerhof functionals, Phys. Rev. B. 59 (1999) 7413–7421. doi:10.1103/PhysRevB.59.7413.

[38] J.P. Perdew, K. Burke, M. Ernzerhof, Generalized Gradient Approximation Made Simple, Phys. Rev. Lett. 77 (1996) 3865–3868. doi:10.1103/PhysRevLett.77.3865.

[39] J. Scaranto, M. Mavrikakis, HCOOH decomposition on Pt(111): A DFT study, Surf. Sci. 648 (2016) 201–211. doi:10.1016/j.susc.2015.09.023.

[40] J. Scaranto, M. Mavrikakis, Density functional theory studies of HCOOH decomposition on Pd(111), Surf. Sci. 650 (2016) 111–120. doi:10.1016/j.susc.2015.11.020.

[41] S. Grimme, J. Antony, S. Ehrlich, H. Krieg, A consistent and accurate ab initio parametrization of density functional dispersion correction (DFT-D) for the 94 elements H-Pu., J. Chem. Phys. 132 (2010) 154104. doi:10.1063/1.3382344.

[42] S. Grimme, Density functional theory with London dispersion corrections, Wiley Interdiscip. Rev. Comput. Mol. Sci. 1 (2011) 211–228. doi:10.1002/wcms.30.

[43] P.E. Blöchl, Projector augmented-wave method, Phys. Rev. B. 50 (1994) 17953–17979. doi:10.1103/PhysRevB.50.17953.

[44] W.M. Haynes, CRC Handbook of Chemistry & Physics, 90th editi, CRC Press, 2009.

[45] G. Henkelman, B.P. Uberuaga, H. Jonsson, A climbing image nudged elastic band method for finding saddle points and minimum energy paths, J. Chem. Phys. 113 (2000) 9901–9904.

[46] G. Henkelman, H. Jónsson, A dimer method for finding saddle points on high dimensional potential surfaces using only first derivatives, J. Chem. Phys. 111 (1999) 7010–7022. doi:10.1063/1.480097.

[47] D. Steele, Infrared Spectroscopy: Theory, in: J.M. Chalmers (Ed.), Handb. Vib. Spectrosc., John Wiley & Sons, Ltd, Chichester, UK, 2006: pp. 3–3. doi:10.1002/0470027320.s0103.

[48] B. Martorell, A. Clotet, J. Fraxedas, A first principle study of the structural, vibrational and electronic properties of tetrathiafulvalene adsorbed on Ag(110) and Au(110) surfaces, J. Comput. Chem. 32 (2009) n/a-n/a. doi:10.1002/jcc.21465.

[49] P. Deshlahra, J. Conway, E.E. Wolf, W.F. Schneider, Influence of dipole-dipole interactions on coverage-dependent adsorption: CO and NO on Pt(111), Langmuir. 28 (2012) 8408–8417. doi:10.1021/la300975s.

[50] J.M. Bray, J.L. Smith, W.F. Schneider, Coverage-dependent adsorption at a low symmetry surface: DFT and statistical analysis of oxygen chemistry on kinked Pt(321), Top. Catal. 57 (2014) 89–105. doi:10.1007/s11244-013-0165-4.

[51] Donald A. McQuarrie, Statistical Mechanics, University Science Books, Sausalito, CA, 2000.

[52] C.T. Campbell, J.R. V Sellers, Enthalpies and Entropies of Adsorption on Well-Defined Oxide Surfaces : Experimental Measurements, Chem. Rev. 113 (2013) 4106–4135. doi:10.1021/cr4003853.

[53] A.F.H. Ward, The sorption of hydrogen on copper. Part I.—Adsorption and the heat of adsorption, Proc. R. Soc. London. Ser. A, Contain. Pap. a Math. Phys. Character. 133 (1931) 506–522. doi:10.1098/rspa.1931.0164.

[54] J.M. Campbell, C.T. Campbell, The dissociative adsorption of H2 and D2 on Cu(110): activation barriers and dynamics, Surf. Sci. 259 (1991) 1–17. doi:10.1016/0039-6028(91)90519-X.

[55] I.E. Wachs, R.J. Madix, The oxidation of H2CO on a copper(110) surface, Surf. Sci. 84 (1979) 375–386. doi:10.1016/0039-6028(79)90143-2.

[56] P. Hollins, J. Pritchard, Interactions of CO molecules adsorbed on Cu(111), Surf. Sci. 89 (1979) 486–495. doi:10.1016/0039-6028(79)90633-2.

[57] W. Kirstein, B. Krüger, F. Thieme, CO adsorption studies on pure and Ni-covered Cu(111) surfaces, Surf. Sci. 176 (1986) 505–529. doi:10.1016/0039-6028(86)90052-X.

[58] M.S. Tameh, A.K. Dearden, C. Huang, Accuracy of Density Functional Theory for

Predicting Kinetics of Methanol Synthesis from CO and CO2 Hydrogenation on Copper, J. Phys. Chem. C. 122 (2018) 17942–17953. doi:10.1021/acs.jpcc.8b06498.